EXPERIMENTAL AND THEORETICAL INVESTIGATION OF FUNCTIONALIZED PEROVSKITES

A Thesis Submitted to
the Graduate School of Engineering and Sciences of
İzmir Institute of Technology
in Partial Fulfillment of the Requirements for the Degree of

MASTER OF SCIENCE

in Photonics Science and Engineering

by
Sercan ÖZEN

July 2020
İZMİR

ACKNOWLEDGMENTS

ABSTRACT

EXPERIMENTAL AND THEORETICAL INVESTIGATION OF FUNCTIONALIZED
PEROVSKITES

The last decade witnessed the rapid increase in the interest of the cesium lead halide perovskites (Cs-LHPs) and their successful applications in optoelectronic devices and photovoltaics. Increasing interest in perovskites arises from their extraordinary features such as having a tunable bandgap, variety in the crystal structure and phases, high photoluminescence quantum yield, ease of synthesis, and wide range absorption spectrum. Desiring to go beyond the emerging findings, subsequent studies have focused on the functionalization of perovskite nanocrystals (PNCs) by dimensional modifications and doping. This thesis study focuses on the modification of characteristics of Cs-LHPs by doping scenarios and dimensional reduction.

Firstly, we reveal the modifications originated from intercalation of Cr^{+3} and Gd^{+3} dopants into the Cs-LHP crystal structures. Cr^{+3} doping process is performed by using room temperature anti-solvent crystallization method. It is observed that the doping process leads to the emergence of distinctive signals in the PL spectrum. We clarify the origin of the each additional PL peaks by experimental measurements and theoretical calculations. Additionally, white light emission is also achieved by the Cr^{3+} doping process. On the other hand, by using hot-injection method, we synthesized neat and Gd^{+3} doped α-$CsPbI_3$ NCs. The stability of α-$CsPbI_3$ NCs is increased by the intercalation of Gd^{3+} ions into the host lattice. Also, enhancement of PLQY and lifetime is achieved by Gd^{3+} doping. Besides, to understand the dopant-induced modifications in the electronic and optical characteristics of perovskites, we also performed *ab-initio* density functional theory (DFT) calculations.

In addition, we study how the characteristic properties of Cs-LHPs are modified upon dimensional reduction. By introducing the electrospraying method we reduced the synthesis and coating processes into a single step. Two-dimensional perovskite nanoplatelets were synthesized by electrospraying. We tuned the emission wavelengths of nanoplatelets in the range of 100 nm by thickness modifications. Lastly, by using DFT, we investigated the effect of thickness-dependent modifications on the structural, electronic, and vibrational properties of the orthorhombic $CsPbI_3$ structure. Phonon calculations show that two ultra-thin forms of bulk $CsPbI_3$ are dynamically stable. Also, the increase in the bandgap energy of the $CsPbI_3$ structure by a decrease in thickness is revealed by electronic band dispersion calculations.

ÖZET

FONKSİYONELLEŞTİRİLMİŞ PEROVSKİTLERİN DENEYSEL ve TEORİK İNCELENMESİ

Son on yıl, sezyum kurşun halojenür perovskitlere (Cs-LHP'ler) olan ilgideki hızlı artışa ve optoelektronik ve fotovoltaiklerdeki aygıtlardaki başarılı uygulamalarına tanık oldu. Bu yapılara olan ilginin artmasının nedeni sahip oldukarı ayarlanabilir enerji bant aralığı, yapı ve faz çeşitliliği, yüksek fotolüminesans kuantum verimliliği, sentez kolaylığı, yüksek taşıyıcı devingenliği ve geniş emilim aralıkları gibi sıradışı özelliklerdir. Perovskitlerin özelliklerinde ortaya çıkan temel bulguların ötesine geçme arzusuyla, sonraki çalışmalar, perovskitlerin fonksiyonelleştirilmesine odaklanmıştır. Bu tez çalışması, katkılama işlemi ve boyutsal modifikasyonlar ile sezyum kurşun halojenür perovskitlerin fonksiyonelleştirilmesine odaklanmıştır.

İlk olarak, Cr^{3+} ve Gd^{3+} atomlarının Cs-ILHP'ler üzerindeki etkileri araştırılmıştır. Katkılama işlemi, fotolümünesans spektrumunda ekstra sinyallere neden olmaktadır. Bu ekstra sinyallerin kökenini deneysel ölçümler ve teorik hesaplamalar ile açıklanmıştır. Bu sinyallerin yoğunluklarında zaman içerisinde meydane gelen değişimin sonucu olarak, beyaz ışık emilimi elde edildi. Öte yandan, Gd^{3+} atomunun sisteme eklenmsi ile $CsPbI_3$ yapısının kararlılığı arttırılmıştır. Katkılanmamış perovskitlerin özelliklerini ve katkılama işleminin sonucunda ortaya çıkan değişiklikleri anlamak için yoğunluk fonksiyoneli teorisine dayalı hesaplamalar gerçekleştirildi.

Ayrıca, Cs-LHP'lerin karakteristik özelliklerinde boyutsal indirgemeye bağlı olarak meydana gelen değişimleri araştırdık. Elektrospreyleme yöntemi ile, perovskit sentezi ve kaplama işlemlerini tek aşamaya indirgenmiştir. Elektrospreyleme yöntemi ile iki boyutlu $CsPbBr_3$ perovskit nano levhalar sentezlenmiştir. Kalınlık modifikasyonlarıyla, nano levhalanrın emisyon dalgaboyları ayarlanabilir hale getirilmiştir. Son olarak, boyutsal modifikasyonların $CsPbI_3$ kristalinin yapısal, elektronik ve titreşimsel özelliklerinde meydana getirdiği değişiklikler, yoğunluk fonksiyoneli teorisi bazlı hesaplamalar ile incelenmiştir. Olası iki ultra-ince yapının dinamik olarak kararlı olduğu fonon hesaplamaları ile ortaya konmuştur. Boyutsal indirgemeye bağlı olarak meydana gelen bant aralığı enerji değerindeki artış elektronik bant dağılımları ile gösterilmiştir.

... to Soner Özen ...

TABLE OF CONTENTS

LIST OF FIGURES

CHAPTER 1

INTRODUCTION

In this age, the rate of renewal of technology has increased considerably. To take civilization to the next level, technology is progressing to an advanced level day by day. However, with a rapid increase in the world population and the increasing use of technology in every aspect of daily life, energy consumption has become one of the most important problems of today. Due to the increase in the energy needs of humanity, this problem has reached to an unignorable level. Considering the exhaustion of non-renewable energy sources and the inability to meet humanity's energy needs, it is clear that renewable energy is the exact solution. Additionally, the consequences of the use of non-renewable energy sources in the past centuries have emerged as air pollution, global warming, climate crisis, and ecosystem imbalances today. Realizing the importance of solving these problems led people to renewable and clean energy sources.

Although this awareness steer humanity to renewable energy sources, we are still using renewable energy resources far below their potential. The tendency to renewable energy sources pointed out problems such as high cost and low efficiency. Therefore, to overcome these issues, scientists have begun to study on different device structures and two-dimensional material variations. Within this search, perovskites have come to the fore as promising materials in the recent past, for the future of energy. Although perovskites bring with it problems related to durability and efficiency, a large area has been opened for both researchers and companies.

Much earlier than these advancements, a calcium titanium oxide mineral was discovered in the Ural Mountains by Gustav Rose in 1839.[1] This mineral is named as perovskite after the Russian mineralogist Lev Perovski and Victor Goldschmidt proposed crystal structure of perovskite for the first time in 1926.[2]

Mostly, the metal halide perovskites composed of a monovalent (A) cation, bivalent (B) cation, and halide (X) anion (typically, Cl^-, Br^-, I^-, or their mixtures) and have the chemical formula ABX_3. Three-dimensional organic-inorganic metal halide perovskites (OIHPs) were first proposed by Weber[3] in 1978 by using organic molecules such as $CH_3NH_3^+$ (MA^+) and $CH_3(NH_2)_2^+$ (FA^+) to occupy A cation and Pb^{+2} as B cation. Two

decades later, OIHPs achieved significant progress thanks to Kagan *et al.* in the last year of the 20th century.[4] After Kojima *et al.* used MAPbX$_3$ perovskites in a solar cell as a photosensitizer, the use of OIHPs in optoelectronic devices has gained steam.[5] By the increasing interest in using hybrid perovskites in optoelectronic devices, %24 power conversion efficiency (PCE) and %20 external quantum efficiency (EQE) was exceeded in solar cells and LEDs, respectively.[6,7,8] In addition, their unusual charge carrier transport properties and high absorption coefficients led to the use of these structures in photodetectors,[9,10] whereas, also detection of gamma rays and X-rays become possible by the presence of Pb atom.[11,12] Despite their salient performances in optoelectronic devices, OIHPs suffer from instability issue. The sensitivity of their organic groups to light, moisture, and heat limits their applications in long-term devices.

Although studies on perovskites have focused on OIHPs, there is a material group that has occurred far before them. In the last decade of the 19th century (1893), Wells reported cesium lead halides and their derivatives by mixing the halides.[13] The synthesis of these now-familiar structures with the chemical formula of CsPbX$_{3-A}$Y$_A$ (X, Y = Cl$^-$, Br$^-$, I$^-$) is first performed by Møller in 1957. Also, he described their crystal structure, phase transition, and photoconductivity.[14,15] In three-dimensional halide perovskites, divalent B-site cations that bridged by halide anions named as metal halide octahedrals. These octahedrals form B-X sublattice in the structure. The cuboctahedral cavities in that sublattice are occupied by a small monovalent A cation that provides charge balance. While Pb^{2+} is mostly used ion as B site cation of IHPs perovskites due to their remarkable optoelectronic properties, K$^+$, Rb$^+$, and Cs$^+$ are frequently used small alkali metal cations that are used to occupy the A site. The tilt or rotation of [PbX$_6$]$^{-4}$ octahedra results in different lattices that described by established nomenclature.[16,17]

All-inorganic halide perovskites (IHPs) have attracted much more attention than OIHPs owing to their superior stability and extraordinary optical and physical properties compared to their hybrid relatives. The study reported by Protesescu et al. in 2015 lit a fire by proposing a synthesis of CsPbX$_3$ nanocrystals with high stability, homogeneous crystal structure, and desired optical properties.[18] Enormous and widespread development of IHPs has encompassed by this resurgence. Attractive results have been obtained thanks to numerous studies carried out to identify and tune the optical, electronic, and structural properties of the all-inorganic perovskites. Their high photoluminescence quantum yield

(PLQY, 90%), narrow emission peak, and tunable bandgap enabled the use of $CsPbX_3$ perovskites in light-emitting diodes, photodetectors, lasing and solar cells.[18,19,20,21,22,23]

Interest in these materials with surprising optical and electronic properties have been increased with each passing day. Their simple and pocket-friendly synthesis that can be carried out with inexpensive systems contributed greatly to the developments in this field. Initially, their phases, chemical compositions, and structural properties were tried to be clarified, and then limits of researches have been expanded. Although they were more stable and efficient compared to OIHPs, they were not suitable for industrial and commercial use in optoelectronic devices yet. After a certain point, studies on IHPs have focused on discovering their unreleased optical and electronic properties and increasing their stability and efficiency. Different strategies such as various synthesis techniques, ligand modification, and doping have been proposed to enhance the structural, optical, and electronic properties of perovskites.

Inserting different atoms that don't belong to the host crystal structure is a well-known process named as doping. The doping process has been used to tune or completely change the optical, vibrational, electronic, and magnetic properties of semiconductors used in device applications.[24,25,26,27,27,28,29,30,31,32] Motivated by the results of the outcomes of the doping strategy in various materials, it has been widely used to tune perovskite's properties and increase their thermal and moisture stability.[33,34,35,36,37] Elements that are used as B-site dopant can be classified into two subgroups. Mn^{2+}, Sn^{2+}, Zn^{2+}, Sr^{2+}, and Ge^{2+} are the mostly used isovalent doping elements.[38,39,40,41,42,43,44] Besides, the mainly used heterovalent doping elements are Eu^{3+}, Al^{3+}, Ce^{3+}, Er^{3+}, Bi^{3+}, Sb^{3+}, Yb^{3+}, Ho^{3+}, Tb^{3+}, and Sm^{3+}.[35,36,45,46,47,48,49,50,51,52,53]

The last decade has witnessed the impetuous progress of researches on doping cesium lead halide perovskites. Studies have revealed that it is possible to tune the optical and electronic properties of perovskite nanocrystals. As well as manipulating the chemical composition by anion exchange[54,55,56,57] or mixed cation,[58,59] their optical and electronic properties can be controlled by intercalation of additional atoms to the crystal lattice.[36,45,46,60,61]

By using the additional ions, it is possible to provide structural perfection, a phase transition, or tuning the bandgap of the material. Besides, additional emission signals can be obtained from dopant induced additional states in the bandgap.[61,62] Pan *et al.* per-

3

formed successful doping processes of $CsPbCl_3$ nanocrystals by using different lanthanide ions and presented the emission spectra differences depending on the dopant ion.[45] Also, Hu *et al.* observed a dual-color emission of $CsPbBr_3$ perovskites by using rare earth elements as a B-site cation dopant.[36] Dual-emission originated from the intercalation of Mn^{2+} ions into the crystal lattice is reported by Liu *et al.*.[63] A shift on the Fermi level in the presence of Bi^{3+} ions is reported by Lozhinka *et al.*[50] By using Bi^{3+} and Mn^{2+} ions, Shao *et al.* obtained white light emission from $CsPbCl_3$ NCs.[64]

Besides tuning the properties of perovskites, a considerable amount of research has focused on increasing their stability against ambient conditions in terms of their use in optoelectronic devices. Introducing additional atoms to the host lattice has been confessed as an effective approach not only to tune optical properties but also to stabilize perovskite nanocrystals.

Stabilization of perovskites through doping have been studied by many researchers to raise the importance of perovskites in the industry. Zou *et al.* proposed a valid Mn^{2+} doping strategy that stabilizes the lattice structure of cesium lead halide perovskite crystals suffering from poor air and thermal stability under ambient conditions.[65] Akkerman *et al.* achieved an increase in the stability of α-$CsPbI_3$ by intercalation of Mn^{2+} ions. Additionally, they showed a shrinking effect of the dopant ion due to the smaller ionic radius on the perovskite lattice that originated from the shortening of the metal-halide bonds by computational works.[38] On the other hand, the contribution of Bi^{3+} heterovalent doping to the stability of α-$CsPbI_3$ is reported by Hu *et al.*.[49] Also, reduced grain size and cubic lattice distortion induced stability increase of Eu^{3+} doped α-$CsPbI_3$ thin films are reported by Jena *et al.*.[51] Dastidar *et al.* presented the surface chloride doping method to increase the moisture stability of $CsPbI_3$ perovskites.[66]

Scientists have developed and studied on many different methods in the search for functionalization of perovskites alongside doping. Within this scope, perovskites of different sizes from quantum dots(QDs) to single crystals(SCs) were synthesized using different synthesis methods. It has been demonstrated that using different methods in the synthesis of perovskites and modifying their dimensions are quite beneficial both in terms of increasing their stability and tuning their optical, electronic, and vibrational properties in line with the area in which the material will be used.

Among IHPs, single crystals have received deserved attention due to their sta-

bility and many researchers have published studies on single crystal cesium lead halide perovskite synthesis in the last decade. By using the Bridgman technique, Stoumpos *et al.* proposed millimeter-scale $CsPbBr_3$ crystals that have the potential to use in X-ray and gamma-ray detection.[67] In 2017, Song *et al.* succeed obtaining 25 cm[3] $CsPbBr_3$ single crystals with high absorption coefficients via the modified Bridgman technique.[68] Apart from the Bridgman method, Dirin *et al.* and Saidaminov *et al.* synthesized $CsPbBr_3$ single crystals using the inverse-temperature crystallization (ITC) method.[69,70] In addition, Rekita *et al.* presented that it is possible to grow $CsPbBr_3$ single crystals by vapor saturation of an antisolvent (VSA).[71]

On the other hand, low-dimensional IHP crystals exhibit significant optical and structural properties and come to fore as promising materials for optoelectronic applications, especially photodetection devices and hetero-structures. Various synthesis strategies for the preparation of IHP NCs have emerged and developed rapidly to synthesize quantum dots, NWs, nanoplatelets, nanocubes, nanosheets, and nanorods. Protesescu *et al.* that the synthesis of CsPbX3 perovskite NCs are possible by hot injection (HI) method where the reaction temperature changes depending on the halide.[18] To produce nanosheets at 150 °C, Shamsi *et al.* dissolved Cs-oleate in oleic acid (OA) and adjusted lateral size control by using octanoic acid and octylamine as surfactants.[72] Additionally, Bekenstein *et al.* synthesized nanocubes at 150 °C, while Zhang *et al.* synthesized 1D nanowires at the same temperature.[73,74] A year after Protesescu's report, through adjusting the surfactants, reaction time, and reaction temperature Sun *et al.* synthesized $CsPbBr_3$ quantum dots, nanocubes, nanorods, and nanoplatelets at room temperature (RT) by using the RT-recrystallization technique.[75]

In addition to the doping process, the fact that the perovskite crystals synthesized in different sizes exhibit different optical, electronic, and structural features increased the interest in the dimension-related changes in the properties of the perovskites.[76,77,78,79] In this regard, in addition to experimental studies, density functional theory based studies have been conducted to investigate and clarify the effects of dimensional modifications in properties of the perovskites. While some scientists have focused on perovskite solar cells,[80,81,82] some scientists investigated structural, optical, electronic, and vibrational properties of perovskites and perovskite-like structures in detail by using density functional theory (DFT) based calculations and simulations. Kawai *et al.* analyzed hot-carrier

lifetimes from electron-phonon interaction by means of first-principles calculations.[83] Using (DFT) calculations, structural, electronic, and vibrational properties of $CsPb_2Br_5$ structure in different dimensions are investigated by Iyikanat *et al.*.[84] Authors have presented that although the Cs atom is essential for the formation of the crystal structure of the $CsPb_2Br_5$, it has no contribution to its electronic structure. Also, it is mentioned that, besides the bulk form of the structure, single layer $CsPb_2Br_5$ structures are also dynamically stable. In 2018, Molina-Sánchez *et al.* reported the correlation between the optical properties of 2D Cs_2PbBr_4 crystal and excitonic effects.[85]

This thesis comprises the results of the functionalization of $CsPbX_3$ (X = Br^-, I^-) perovskite structures by heterovalent doping and dimensional modifications. The experimental results of the studies carried out within the scope of this master's thesis were examined using absorption and photoluminescence spectroscopy techniques, scanning electron microscopy (SEM), scanning transmission electron microscopy (STEM), X-ray diffraction, photoluminescence quantum yield (PLQY), and lifetime measurements. In order to support and to get a deeper insight into the physics behind the outcomes, originated from modifications, DFT based atomic calculations, and simulations were performed.

Cr^{3+} driven single-phase white light emission with quite high CRI obtained by two-step room temperature synthesis. Further, multiple PL peak regions originated from the anion-exchange and the presence of Cr^{3+} were investigated. By using the hot injection method, stability of α-phase $CsPbI_3$ at room temperature is increased by intercalation of Gd^{3+} ions to the host lattice in different molar ratios. In addition, due to the decrease in defect density, PLQY and fluorescence lifetime of $CsPbI_3$ perovskite structure are increased. Both doping scenarios and effects of dopant ions on the electronic structure of perovskites are investigated by using DFT based calculations. Moreover, a facile and novel synthesis method, electrospraying is presented. $CsPbBr_3$ perovskite nanoplatelets with tunable optical properties are synthesized by this technique. Furthermore, structural, optical, electronic, and vibrational properties of various $CsPbI_3$ structures in different thicknesses were investigated on the basis of the DFT based calculations to understand the modifications originated from the size effect.

CHAPTER 2

METHODOLOGY

2.1. Experimental Methodology

2.1.1. Cesium Lead Halide Perovskite Synthesis

Brief information about various perovskite synthesis methods that are used during this thesis study is given in this subsection.

2.1.1.1. Chemicals and Equipment

Cesium bromide (CsBr, 99.9 %), lead(II) bromide ($PbBr_2$, 98 %), lead(II) iodide (PbI_2, 99 %), chromium(III) chloride ($CrCl_3$, 99.9 %), cesium carbonate (Cs_2CO_3, 99.9%), gadolinium acetate ($Gd(CH_3CO_2)_3xH_2O$, 99.9 % trace metal basis), 1-octadecene (ODE, 90%), oleylamine (OLAM, 70%), and oleic acid (OA, 90 %), Hexane (98 %) were purchased from Sigma-Aldrich. Toluene ($\geq$99 %) and N,N-dimethylformamide (DMF, 99.9 %) were purchased from Merck and Tekkim respectively. All reagents were used as received without any further purification.

1.3 mm inner diameter plastic syringe with stainless-steel needle (21G$\times$1 1/2, Interlab), single-channel programmable syringe pump (SyringePump, NE-1000), power supply (Gamma H. V. Research Ormond Beach, FL), 1 in^2, ITO coated glasses obtained by cutting 3 in^2 ITO coated glasses (Rs$<$10 Ω/sq., Teknoma). ITO coated glasses are cleaned first with sponge and dish soap without damaging the ITO layer. After that, 5 minutes of sonication in ethanol followed by washing with acetone and then with distilled water. Finally, substrates are treated with N_2 flow for one minute.

2.1.1.2. Room Temperature Synthesis Method

Preparation of Precursor Solution: The room temperature synthesis of cesium lead bromide perovskite nanocrystals was performed by following the method proposed by Li *et al.*.[86] 0.4 mmol of each CsBr and $PbBr_2$ salts were dissolved in 10 mL dimethyl-formamide (DMF) under vigorous stirring in a glass vial. After complete dissolution of salts, 1.0 mL OA and 0.5 mL OLAM were added as surfactants and stirred for 10 minutes.

Preparation of Dopant Source: 0.8 mmol of $CrCl_3$ was completely dissolved in 10 mL of DMF under vigorous stirring at room temperature.

Crystallization of Doped and Undoped Perovskite Nanocrystals: 5 mL toluene loaded glass vial placed on the magnetic stirrer. 0.5 mL of precursor solution, was dropped into toluene under vigorous stirring. To obtain doped perovskite NCs, the method proposed by Zhu *et al.* was followed with slight modifications.[87] 0.5 mL of precursor solution and 0.5 mL of dopant solution were dropped into the toluene at the same time under vigorous stirring. After 3 minutes, the reaction was terminated by stopping the stirring. The final solution was centrifuged at 6000 rpm for 10 minutes and precipitated crystals are dispersed in hexane for further use.

2.1.1.3. Hot-Injection Method

Neat and Gd^{3+} doped $CsPb_xGd_{1-x}I_3$ nanocrystals were synthesized by following the hot injection method described by Protesescu et al.[18]

Synthesis of Cs-oleate Solution: Oleic acid (OA); 2.5 mL, octadecene (ODE); 40 ml, cesium carbonate (Cs_2CO_3); 0.814 g were loaded into 3-neck flask and heated to 120 °C under vacuum and vigorous stirring for degassing. After the 1 hour of degassing at 120 °C, the temperature increased to 150 °C under N_2 flow. Two hours later, a yellowish Cs-oleate solution that is the cesium source for the second step is obtained. Since it precipitates out of ODE at room-temperature, the Cs-oleate solution was pre-heated to 100 °C before use.

Synthesis of Doped and Undoped Perovskite Nanocrystals: A glass tube containing 5 mL ODE and 0.188 mmol PbI_2 dried under vacuum and vigorous stirring for 1 hour at 120 °C. For doped nanocrystals, different amounts of $Gd(Ac)_3$ were added. Af-

ter degassing, 0.5 mL oleylamine (OLAM) and 0.5 mL OA were injected under N_2. By the complete dissolution of the salt, the temperature was raised to value in the range of 140 - 200° C for tuning the nanocrystal size. Then, 100 μL of Cs-oleate (pre-heated to 100°C) was injected into the 3-neck flask and the solution was quenched by an ice-water bath 5 seconds after the injection. At last, the mixture was centrifuged and perovskite nanocrystals redispersed in toluene for further use.

Degassing process described above for the Cs-oleate solution is repeated for a glass tube containing 1.25 mL of ODE, 125 μL of OA, and 125 μL of OLAM and then, the temperature was increased to 150 °C under N_2 flow. Subsequently, a 100 μL Cs-oleate solution preheated to 100 °C is swiftly injected into the glass tube. After 10 seconds from the injection, the glass tube removed from the setup and immediately quenched by using a water-ice bath. After that, the nanocrystal solution is centrifuged at 6000 rpm for 15 minutes and precipitated nanocrystals were redispersed in toluene for further use.

2.1.1.4. Electrospraying Method

Preparation of Precursor Solution: For preparing the precursor solution of electrospraying technique, slight modifications were applied on the recipe proposed by Li *et al.*.[86] 0.08 M DMF solution including equal amounts of CsBr and $PbBr_2$ salts were stirred until the full dissolution of salts and different amount of ligands (OA and OLAM) were added to tune the dimension of perovskite nanoplatelets that will be obtained in fabrication.

Fabrication of Perovskite Film on Substrate: 1.3 mm inner diameter plastic syringe was loaded with a 0.4 mL precursor solution and placed on to programmable syringe pump (SyringePump, NE-1000). The distance between 1 in^2, ITO coated glasses (Rs<10 Ω/sq., Teknoma) and the tip of the stainless-steel needle (21G×1 1/2, Interlab) was set to be 16 cm. For electrospraying, different amount of DC voltage (5, 10, 15, 20 kV) was applied to the needle by a power supply (Gamma H. V. Research Ormond Beach, FL). The optimal voltage applied to the needle and the flow rate of the precursor solution was determined as 20 kV and 1.5 mL/s respectively.

2.1.2. Characterization Techniques

This subsection comprises detailed information about the characterization techniques used during this thesis study.

2.1.2.1. UV-Vis Absorption Spectroscopy

In semiconductor physics, the bandgap is the forbidden region for electrons to exist and the energy of the bandgap is defined by the energy difference between valance band maximum (VBM) and the conduction band minimum (CBM) of the material. All materials have a unique electronic band diagram. Instead of the position vector, VBM and CBM of a material are defined by crystal momentum, represented as wave vector K, in energy-momentum space. If the maximum energy state of the valance band and the minimum energy state of the conduction band of a material possess at the same momentum value, direct transition is allowed and the material is direct bandgap semiconductor. However, VBM and CBM of an indirect bandgap semiconductor have different momentum values and the ΔK is large. Thus, direct transition is not allowed. For a transition in a semiconductor, an electron in the valance band must be excited by an external factor (e.g. illumination, current etc.). When the amount of energy gained by electron through the excitation is larger than the bandgap energy of the material, the excited electron occupies an excited stated in the conduction band. This process is called absorption.

Considering photovoltaic or light-detecting devices, the absorption properties of a material are crucial. The fundamental information about the material can be obtained by absorption spectroscopy in terms of wavelength, frequency, or energy. Under the illumination, as the material transmits a portion of the light with the energy lower than its bandgap energy, it absorb photons with equal and higher energy than its bandgap energy.

Similar to bandgap energies and band alignments, semiconductors have different absorption coefficients. This coefficient determines the penetration depth of light of a particular wavelength into a material. Light is poorly absorbed by a material with a low absorption coefficient. However, a higher amount of light would be absorbed by materials with higher absorption coefficient. Therefore, before designing an optoelectronic device, the absorption coefficient is crucial to determine the material to use as a light absorber.

To calculate the absorption coefficient, (α), of a material with the thickness t, the formula below is used;

$$\alpha = (2.303 x A_b)/t \tag{2.1}$$

where A_b is the absorption. By the absorption coefficient, one can evaluate the optical bandgap of the thin film by using Tauc Plot technique. The equation of Tauc plot for the incoming photon with the energy of $h\nu$ is;

$$\alpha h\nu = \alpha_0 (h\nu - E_g)^n \tag{2.2}$$

where α_0 is a constant, E_g is the bandgap energy and n is a special parameter depending on the type of the material such as $1/2$, 2, $3/2$ and 3 for allowed direct, allowed indirect and forbidden direct and forbidden indirect transitions respectively. A linear line drawn through the exponential part of the Tauc plot intersects the x-axis at the optical band edge value and gives the optical bandgap or Tauc-gap value in terms of energy.

On the other hand, UV-Vis absorption spectroscopy can be used to obtain information about the crystal structure. Structural disorder and imperfections result in localized states in the bandgap. Therefore, a large exponential part appears along the absorption coefficient curve of low crystalline, disordered, and amorphous structures (near the optical band edge). This curve is also called the Urbach tail.

Urbach energy has an inverse relation with crystal quality. By using this relation, it is possible to investigate the effects of applied modifications on the crystal quality. For example, if the Urbach energy is getting smaller related to the increasing dopant ratio, it can be said that the doping increases the crystallinity and decreases the disorder of the structure.

Urbah energy E_U can be obtained by using the absorption coefficient α and photon energy ($h\nu$);

$$\alpha = \alpha_0 exp(h\nu/E_U) \tag{2.3}$$

where α_0 is a constant. The logarithm of the two sides of the Eq. 2.3, gives a straight line equation;

$$ln\alpha = ln\alpha_0 + (h\nu/E_U) \tag{2.4}$$

Therefore, Urbach energy (E_U) can be obtained from the slope of the straight line of plotting $ln\alpha$ versus the incident photon energy ($h\nu$).

11

2.1.2.2. Photoluminescence

Emission of light that is not originated from heat is called luminescence. There are different luminescence types classified due to the source initiating the process such as photoluminescence, electroluminescence, radioluminescence, chemiluminescence, cathodoluminescence, mechanoluminescence, and thermoluminescence. All of these luminescence processes play an important role in scientific studies and industry. For example, electroluminescence, in which applying an electric field across a material results in electron-hole recombination triggered light emission is crucial for characterization of light-emitting diodes; and for detection of poison in air chemiluminescence, light emission originated from a chemical reaction is used.
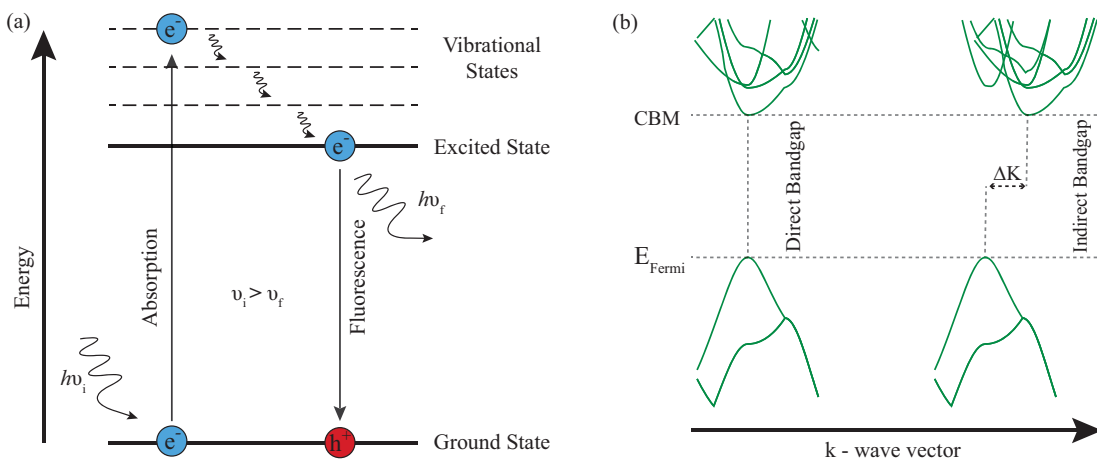
Figure 2.1. (a) Energy diagram, (b) direct and indirect bandgap diagrams.

Among these techniques, photoluminescence (PL) spectroscopy is a non-destructive and fundamental spectroscopy technique that is frequently used in both scientific studies and industry. The term photoluminescence covers phosphorescence and fluorescence. Phosphorescence is a delayed release of absorbed electromagnetic radiation. In fluorescence, when external radiations fall on to the material, it absorbs energy. Due to the characteristic structure of the material, only radiation of specific energy can be absorbed. This absorption triggers an electronic transition to higher states. Excited electron occupies the excited state for a certain time like 10^{-8} to 10^{-4} seconds, but it is not stable at excited states. So electron wants to turn back to its ground state and to recombine with

a hole. This transition is called relaxation or electron-hole recombination and involves less energy than absorption since the excited electrons lose a small amount of their energy as heat due to the atomic vibrations in molecules. This transition can be radiative or non-radiative. In the non-radiative case, since the CBM and the VBM do not pose at the same momentum value, ΔK is very large and an electron has to make an oblique transition. Since this is permitted by selection rule, the energy difference is given in terms of phonon. If the CBM and the VBM pose at the same K value, a vertical transition occurs and during this transition, the energy is released in terms of a photon, and this process is called fluorescence. Emission of photons can be originated from the crystal itself or defect states. Therefore, photoluminescence spectroscopy is of great importance in obtaining information about the optical properties of materials especially in the optoelectronic device area.

2.1.2.3. Scanning Electron Microscopy

One of the most important parts of the characterization of perovskite structures is optical screening. It is possible to see whether there are nanocubes, nanowires, or nanoplatelets. In order to create an image, a scanning electron microscope (SEM) scans the surface by using a focused electron beam. As a result of the interaction of the beam and the surface, secondary electrons (elastically scattered electrons, SE) and backscattering electrons (in-elastically scattered electrons, BSE) are collected by corresponding detectors. The image created by collecting the scattered electrons provides important information about grains, crystal dimensions, crystallization direction, and crystallization orientation. Besides, some samples were examined in STEM (Scanning Transmission Electron Microscope) mode. In this mode, as in the SEM, a focused beam scans the sample but, the image is generated by transmitted electrons. In addition, the electron vacancies after the interaction of the beam and the sample are filled with electrons of a higher state. To balance the energy difference between two states, atoms emit characteristic x-ray that is used for elemental identification and mapping. Since the x-ray energy of each element is unique, it is used for elemental analysis especially for doped samples to identify the content of the material.

In this work, Philips XL 30S FEG, FEI QUANTA 250 FEG, and Zeiss Evo 10

scanning electron microscopes in the İzmir Institute of Technology, Center for Materials Research are used. Since the work includes semiconductor materials, there was no necessity for any coating processes.

2.1.2.4. X-Ray Crystallography Diffraction Spectroscopy

X-ray diffraction is a technique based on the diffraction of incident X-rays by the sample. When crystalline samples exposed to the X-rays, they act as diffraction gratings depending on the spacing of planes in it and cause X-rays to diffract into many directions. When the conditions specified by Bragg's Law are satisfied, a constructive interface occurs as a result of the interaction between the incident rays with a sample. The angle between the incident and diffracted rays is the key parameter of X-ray diffraction. This angle is related to the lattice spacing (d-spacing) in a crystal by Bragg's Law. To identify the sample's chemical composition, the mean position of atoms, bonds, crystallographic disorder, and recognition of crystalline phases, X-ray diffraction is a commonly used characterization technique.

In this work, Philips X′Pert Pro X-Ray Diffractometer in the İzmir Institute of Technology, Center for Materials Research is used.

2.2. Computational Methodology

2.2.1. Density Functional Theory

This section comprises fundamentals of, one of the most used methods, a computational quantum mechanical modeling method DFT, to understand the matter in the view of ground-state electronic structure, electronic, magnetic and vibrational properties.

2.2.1.1. Fundamentals of Density Functional Theory

Information about the properties of any system is enclosed by its quantum mechanical wave function. Wave function can be obtained by solving the wave equation,

which is Schrödinger equation for non-relativistic systems. For simple systems such as hydrogen atom or 2D square potential, the Schrödinger equation can be solved easily.

The mathematical expression for the wave function of any system can be represented by the non-relativistic time-dependent Schrödinger equation

$$\hat{H}\Psi = E\Psi \tag{2.5}$$

where the operator $\hat{H}$ is the energy operator known as the Hamiltonian and the E is the corresponding eigenvalue for the Hamiltonian operator. The wave function Ψ, the solution of the Eq. 2.5 are the eigenfunctions of the Schrödinger equation.

However, when more complex systems need to be understood, the Scrödinger equation becomes more complex for many-body systems, and it is almost impossible to solve this equation. For a many-body system with M nuclei and N electrons, the non-relativistic many-body $\hat{H}$ has the general form of;

$$\hat{H} = -\frac{\hbar^2}{2m_e}\sum_i^N \nabla_i^2 + \frac{e^2}{4\pi\epsilon_0}\left[-\sum_i^N\sum_I^N \frac{Z_I}{|\mathbf{r_i} - \mathbf{R_I}|} + \frac{1}{2}\sum_i^N\sum_{j\neq i}^N \frac{1}{|\mathbf{r_i} - \mathbf{r_j}|}\right. \tag{2.6}$$

$$\left.+\frac{1}{2}\sum_i^N\sum_{J\neq I}^N \frac{Z_I Z_J}{|\mathbf{R_I} - \mathbf{R_J}|}\right]$$

The first and the second terms stand for the kinetic energy of the system in terms of the electrons and nuclei. The Coulomb repulsion between electrons and nuclei is included by third and fourth terms respectively. The last term of the equation represents the Coulombic interaction between the electrons and nuclei.

Unless quantum computers are used, solving the Eq. 2.5 for such a large system would be almost impossible. Therefore, the introduction of approaches to solve the problem and attain information about the system is necessary. Density Functional Theory is one of the most common quantum mechanical methods to obtain an approximate solution to the Shrödinger equation of a many-body system. DFT defines an interacting many-body system as a functional of the ground state density that is a function of the position. By this approach structural, electronic, optical, magnetic, and vibrational properties of many-body systems can be investigated.

2.2.1.2. Hohenberg-Kohn Theorems

In 1964, Hohenberg and Kohn made DFT possible by proving the existence of universal functional of density. In other words, for a quantum many-body system, its ground state energy can be explained as a density functional. Their approach resulted in adroitly proposed two fundamental theorems; (i) there is one-to-one matching between densities and external potential for any system of interacting particles in an external potential $V_{ext}(\mathbf{r})$, (ii) The total energy ($E[n]$) can be defined as a functional in terms of density. This functional has its global minimum value at the exact ground state energy of the system. The exact ground state density $n_0(r)$ is the density that minimizes the functional. In terms of the ground state wave function, the ground state energy can be written as the expectation value of the Hamiltonian and V_{ext} becomes,

$$E = \frac{\langle \Psi_0 | H | \Psi_0 \rangle}{\langle \Psi_0 | \Psi_0 \rangle} \equiv \langle H \rangle = \langle T \rangle + \int d^3\mathbf{r} V_{ext}(\mathbf{r}) n_0(\mathbf{r}) + \langle V_{int} \rangle + E_{II} \qquad (2.7)$$

2.2.1.3. Hellmann-Feynman Theorem

Hellmann and Feynman evaluated this theorem to its last form and indicated that forces acting on the nucleus in a system and electrostatic forces exerted on the nucleus by the other nuclei and the charge density of the electron exchange and correlation are relatable. For a Hamiltonian which is a function of parameter λ with eigenfunction $\Phi(\lambda)$ and eigenvalue E(λ) derivative of the E with respect to λ is equal to the expectation value of the derivative of the $\hat{H}$ with respect to the λ and the minimum energy corresponds to the zero force. In this regard, Hellmann - Feynman Theorem is essential for DFT based calculations. Also, derivation can be generalized to any parameter, the force in the Hamiltonian conjugates to any parameter.

$$\mathbf{F}_I = -\frac{\partial E}{\partial \mathbf{R}_I} \qquad (2.8)$$

Since the force depends on the density of electrons, n, and the other nuclei, when one considers Eq. 2.7 and Eq. 2.8 the force becomes,

$$\mathbf{F}_I = -\frac{\partial E}{\partial \mathbf{R}_I} = -\int d^3\mathbf{r}n(\mathbf{r})\frac{\partial V_{ext}(\mathbf{r})}{\partial \mathbf{R}_I} - \frac{\partial E_{II}}{\partial \mathbf{R}_I} \qquad (2.9)$$

2.2.1.4. The Kohn-Sham Equations

The Hohenberg-Kohn theorem based method minimizing the energy functional by varying the charge density over all densities is proposed by Walter Kohn and Lu Jeu Sham in 1965.

The sum of kinetic energy of non-interacting electrons, $T[n]$, Hartree energy, $E^{Hartree}$, and exchange and correlation energy, E_{xc}, is used to define the universal functional $F_{HK}[n]$, and the energy functional takes the form,

$$E[n] = \int n(r)V_{ext}(r)dr + F_{HK}[n] = \int n(r)V_{ext}(r)dr + T[n] + E^{Hartree}[n] + E_{xc}[n]$$
$$(2.10)$$

It is crucial to define an effective potential which has the form,

$$V^{eff} = \frac{\delta\{\int n(r)V_{ext}(r)dr + E^{Hartree}[n] + E_{xc}[n]\}}{\delta n(r)}, \qquad (2.11)$$

and that equation shapes into the form,

$$V^{eff} = V_{ext}(r) + \int \frac{n(r')}{|r-r'|}dr' + V_{xc}(r), \qquad (2.12)$$

where $V_{xc}(\mathbf{r})$ is the exchange-correlation potential derived from the exchange-correlation energy.

The form of V^{eff} is implemented to the Schrödinger equation in Kohn-Sham DFT and one electron Schrödinger like equation is obtained.

$$\left[-\frac{1}{2}\nabla^2 + V^{eff}\right]\phi_i = E_i\phi_i \qquad (2.13)$$

where the eigenfunctions, ϕ_i, are the Khon-Sham one-electron orbitals that result in the electron density,

$$n(r) = \sum_{i=1}^{N} |\phi_i|^2 \qquad (2.14)$$

Since the effective potential, V^{eff}, depends on the density, $n(r)$ due to the form of Eq. 2.14, the Kohn-Sham equation should be solved by following a certain process. Construction of effective potential, V^{eff}, requires an initial guess of the electron density. Then Khon-Sham orbitals, ϕ_i corresponding to this V^{eff} is obtained. Lastly, present electron density is compared to the previous one. When the convergence is achieved at this loop, the total energy can be calculated in terms of the final electron density. Even if the final electron density is obtained by this process, the exchange correlation energy is still not included.

2.2.1.5. Functionals of Exchange and Correlation

The necessity of exchange-correlation functional to solve the Kohn-Sham equation and the absence of the exact expression for this functional give arise to introduction of approximations. Two mostly used approximations, LDA (Local Density Approximation) and GGA (Generalized Gradient Approximation) are mentioned in this chapter.

Local Density Approximation (LDA) : Local Density Approximation (LDA) is the simplest approximation introduced by Kohn and Sham and holds for the systems with slowly varying density. In this approximation, the exchange-correlation energy is approximated by the exchange-correlation functional of homogeneous electron gas of the same density. The exchange-correlation energy is described by the formula;

$$E_{xc}^{LDA}[n] = \int n(r)\epsilon_{xc}^{unif}[n]dr \qquad (2.15)$$

with exchange-correlation energy per electron; ϵ_{xc}^{unif}.

This basic approximation, which lies behind the most of the modern DFT codes, provides quite accurate results. It works well for metallic systems however, binding energies are overestimated as the ionization and ground state energies are underestimated within this approximation.

Generalized Gradient Approximation (GGA) :

The LDA was insufficient for systems with rapidly changing electron densities and therefore $\nabla n(r)$; the gradient of the electron density is introduced. Since GGA func-

tionals are dependent on the electron density gradient, they are known as semi-local functionals. Exchange-correlation energy for the total energy functional in GGA is defined as;

$$E_{xc}^{GGA}[n] = \int f^{GGA}(n(r), \nabla n(r)) dr \qquad (2.16)$$

2.3. Computational Details

This section includes the methods, input parameters and approaches used in computational calculations and simulations. Theoretical investigation of structural and electronic properties of perovskites were performed by using Vienna *ab-initio* Simulation Package (VASP).[88,89] VASP uses the plane wave basis set to solve the Kohn-Sham equations[90] and computes an approximate solution to the many-body Schrödinger equation of the system with periodic boundary conditions. To simulate the interaction energy between the core and valance electrons, and to treat electron exchange-correlation energy, plane-wave projector augmented wave (PAW)[91,92] pseudopotential datasets were used as implemented in VASP. The exchange-correlation potentials are approximated by using generalized gradient approximation (GGA) in the form of Perdew-Burke-Ernzerhof (PBE)[93] functional and local density approximation (LDA).[94] Inadequacy of GGA approximation in considering the van der Waals (vdW) forces were ameliorated by using the DFT-D2 method of Grimme.[95] The charge donated and received by atoms was calculated by using Bader technique.[96] The stability of the structures against temperature was also examined using molecular dynamics (MD) simulations. Additionally, phonon band dispersions were calculated by using the PHONOPY code to investigate the dynamical stability.[97]

The input parameters used for optimization of the structures are as follows. For all calculations, the kinetic energy cutoff for plane-wave expansion was set to 500 eV. Total energy difference convergence criterion for self-consistent calculations was set to be 10^{-5} eV to reach the exact ground state of the system. Also force acting on the unit cell is reduced to a value less than $|1|$ kB in all directions. For the determination of accurate charge densities, Brillouin Zone integration was performed using various Γ-centered k-point meshes. Gaussian smearing of 0.1 eV was used for bulk structures and 0.05 eV for

single and bilayer structures electronic density of states calculations.

We also calculated the cohesive energy (E_{coh}) per atom by using the formula;

$$E_{Coh} = \Big[\sum_i n_{atom(i)} E_{atom(i)} - E_{system} \Big] / n_{total} \tag{2.17}$$

where ground state energy of the system and single atom energies are E_{system} and $E_{atom(i)}$ for the ith atom respectively. n_{total} represents the total number of atoms, and $n_{atom(i)}$ shows the numbers of same kind of atoms in the unit cell.

Parameters that vary according to structures are given in the relevant sections.

CHAPTER 3

FUNCTIONALIZATION OF CESIUM LEAD HALIDE PEROVSKITES BY DOPING

Cesium lead halide perovskites have attracted significant attention as a promising class of semiconductors for new age optoelectronic devices. These strong contenders of optoelectronic device applications exhibit outstanding properties such as tunability of bandgap, narrow full width half maximum (FWHM) emission peak, high PLQY, large absorption spectrum, high defect tolerance, long carrier lifetime, and high charge carrier density.[18, 19, 20, 21, 22, 55, 98, 99, 100]

After understanding the basic properties of perovskites and studying different synthesis methods of various perovskite structures, investigative efforts have turned to the functionalization of these promising materials. We can divide the different strategies used to functionalize the cesium lead halide perovskites into four different groups; (i) ligand modifications, (ii) anion exchange, (iii) doping, and (iv) dimensional modifications. By ligand modifications, scientists have tuned the optical properties of perovskites by modifying the thickness of the crystal structure, tuned the structure of the perovskite nanocrystals, and increased stability of perovskite nanocrystals.[75, 77, 100, 101] On the other hand, with a different approach, using anion exchange, $CsPbBr_xCl_yI_z$ structures containing different ratios of Cl^- Br^-, and I^- ions were synthesized and the tunability of optical and electronic properties of perovskites was achieved.[18, 19, 22, 55, 102]

Among these strategies, the doping process has become the most studied strategy that is used to tune or completely change the optical and electronic properties of perovskite nanocrystals. Many researchers have used different types of atoms as a dopant to tune the optical and electronic properties of perovskites. Studies have revealed that, emission color and Fermi level of the perovskite structures can be tuned, additional emission peaks in the PL spectra and single-phase white light emission can be obtained by doping strategy.[36, 45, 50, 63, 64]

On the other hand, for perovskites to be suitable for commercial use, how stable they are against external conditions is a point to be considered. In the functionalization of perovskites, increasing their stability is at least as important as tuning their optical and

electronic properties.

Among cesium lead halide perovskites, $CsPbI_3$ stands out for optoelectronic device applications. This structure possesses high thermal stability and ~ 1.7 eV bandgap which is desirable for light detecting devices such as photodetectors and photovoltaic cells.[103, 104] However, although α-$CsPbI_3$ (black phase) perovskites are stable at high temperatures ($\geq 320\ ^\circ$C),[105] they are metastable at room-temperature and unable to maintain their structure. Unfortunately, the phase transition from α-$CsPbI_3$ to δ-$CsPbI_3$ non-perovskite orthorhombic structure which is also called the yellow phase is inevitable.[20, 103] To prevent the phase transition in order to use promising properties of α-$CsPbI_3$ in optoelectronic devices, researchers have focused on increasing the stability of α-$CsPbI_3$ perovskite structure by ligand modifications and various doping scenarios.[33, 37, 38, 39, 41, 66, 102, 106]

3.1. Tuning the Optical Properties of CsPbBr$_3$ Perovskites by Doping and Anion Exchange

In this section, procedures and results of heterovalent doping of cesium lead bromide perovskite crystals are presented. Neat and Cr^{3+} doped $CsPbBr_3$ perovskites were synthesized at room temperature by following a facile route involving an antisolvent recrystallization method. In order to understand the effects of the doping process on the nanocrystals, various amounts of $CrCl_3$ dopant solution were used. By the intercalation of Cr^{3+} and Cl^- ions into the $CsPbBr_3$ crystal lattices, distinctive peaks were observed in the PL spectrum. Experimental measurements and the DFT based calculations reveal that additional signals originated from $CsPbBr_xCl_{3-x}$ crystal domains, Cr-strained host lattices, and dopant induced midgap states. Also, single-phase white light emission with quite high CRI (88) is obtained in a 30-day time interval.

Details about the chemicals and the synthesis of neat and Cr^{+3} doped $CsPbBr_xCl_{3-x}$ nanocrystals defined in subsections 2.1.1.1 and 2.1.1.2 respectively. In this work, deuterium-tungsten light source (DH-2000-BAL), USB2000+ spectrometer (Flame-T-XR1-Es) and fiber cables (Ocean Optics Inc., Dunedin, FL, USA) in the CENT Research Group Laboratory are used for absorbance and photoluminescence measurements.

For the DFT based calculations of neat and Cr^{3+} doped $CsPbBr_xCl_{3-x}$ crystals, exchange-correlation potentials are approximated by using LDA[94] and the kinetic en-

ergy cutoff for plane-wave expansion was set to 500 eV. For the determination of accurate charge densities, Brillouin Zone integration was performed using Γ-centered k-point meshes of $3\times3\times3$. Gaussian smearing of 0.1 eV was used for all structures. Comprehensive information about computational methodology is given in section 2.3.

3.1.1. CrCl$_3$-Driven Modifications in the Atomic Structure

The differences in the optical, electronic, and vibrational properties of the material arise as a result of modifications in the crystal symmetry. Therefore, understanding the structural properties of the material is crucial. Our undoped, and 0.25mL, 0.50 mL, and 0.75 mL dopant solution injected samples are labeled as Cr0, Cr25, Cr50, and Cr75, respectively. Our neat sample has orange color under daylight. Following the inclusion of CrCl$_3$ solution, the color of the doped samples under the daylight shift from orange to yellowish and then to whitish color as the amount of CrCl$_3$ solution increases. Moreover, under UV illumination ($\lambda = 254nm$), the bright green emission of the neat sample shows a significant shift toward violaceous color by the increase in the amount of dopant solution. However, even if the amount of CrCl$_3$ solution increases, almost there is no visible difference to the naked eye between the emission color of the doped samples.

Crystals have distinctive spacings between planes. Therefore, it is possible to characterize the crystal's structural properties by using X-ray diffraction. The XRD pattern of the neat sample presents sharp signals compatible with the Cs$_4$PbBr$_6$ structure.[107] Signals that matches with the Cs$_4$PbBr$_6$ perovskite structure are labeled with "*". As the CrCl$_3$ solution introduced, extra reflections that match well with the CsPbBr$_x$Cl$_{3-x}$ has appeared in the XRD pattern of doped samples. The reflection signals of CsPbBr$_x$Cl$_{3-x}$ structure are marked with dashed lines.[18] As the CrCl$_3$ concentration increases, some of the Cs$_4$PbBr$_6$ signals remain, however, X-ray diffractogram is dominated by the signals of CsPbBr$_x$Cl$_{3-x}$ crystal. Moreover, the shift towards higher θ values indicates the shrinkage of the structure due to anion exchange and Cr^{+3} incorporation.[55]

To visualize the crystal structure of the neat and doped perovskite crystals, samples were characterized by SEM imaging. The SEM images of samples Cr0 and Cr75 are given in Fig. 3.2. It is seen that the undoped sample consists of two different structures with cubic and rhombus shapes. Those shapes were highlighted with green and

yellow lines, respectively. Compatible with the XRD measurements, the undoped sample is composed of rhombus-shaped Cs_4PbBr_6 crystals and the presence of $CrCl_3$ leads to the formation of a significant amount of crystals in the cubic phase indicating the formation of $CsPbBr_xCl_{3-x}$ nanocrystals.
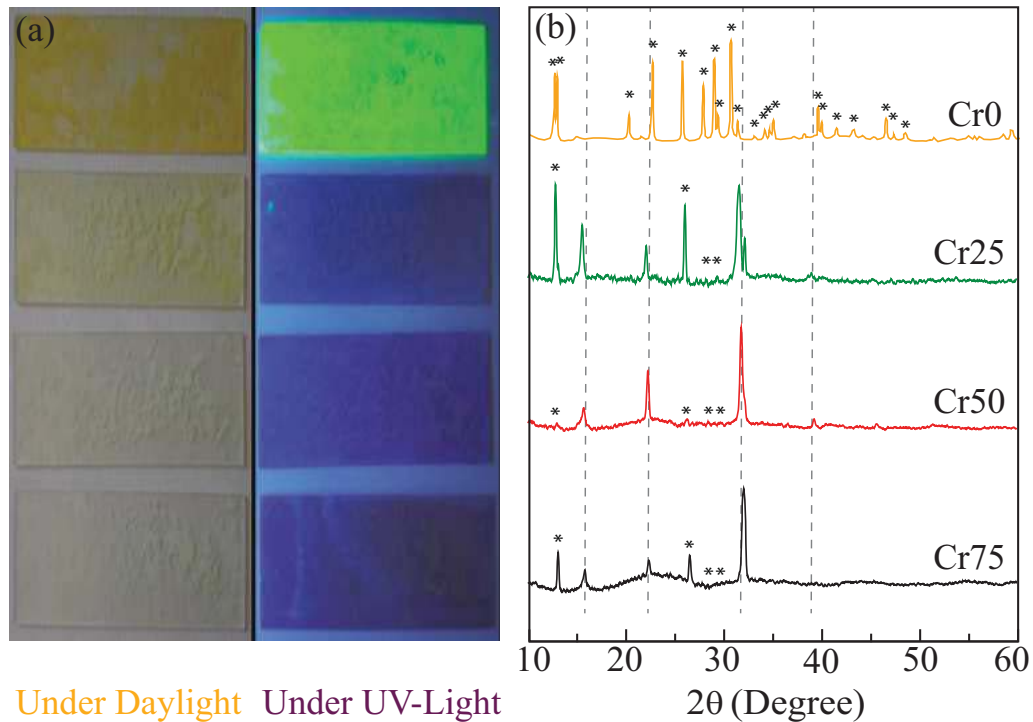
Figure 3.1. (a) Photographic images under daylight and UV-light and (b) X-ray diffraction patterns of Cr0, Cr25, Cr50, and Cr75 samples.[108] Reprinted with permission from Ozen *et al.* J. Appl. Phys. 125(22):225705 2019. Copyright 2019 AIP Publishing.

In the doping scenarios, it is crucial to clarify whether the structure is doped or not. Besides, in cases involving both anion exchange and doping, origin of the modifications should be identified. To identify the sample's chemical composition, energy dispersive X-ray (EDX) analysis is performed. The intensive amount of Cs^+ and Br^- atoms in the undoped sample indicates the formation of Cs_4PbBr_6 while Cr75 possesses relatively close amounts of Cs^+ and Br^- atoms. Results also prove the presence of Pb^{2+} atom in both structures and Cr^{3+} and Cl^- atoms in the doped samples. All Cr-doped samples contain various amounts of Cl^- because of the higher electronegativity of Cl^- compared to Br^-. Based on the EDX results, the stoichiometric ratios for the samples Cr25, Cr50, and Cr75 are $CsPbBr_{1.41}Cl_{1.59}$:Cr, $CsPbBr_{0.93}Cl_{2.07}$:Cr, and $CsPbBr_{0.69}Cl_{2.31}$:Cr respectively.

24
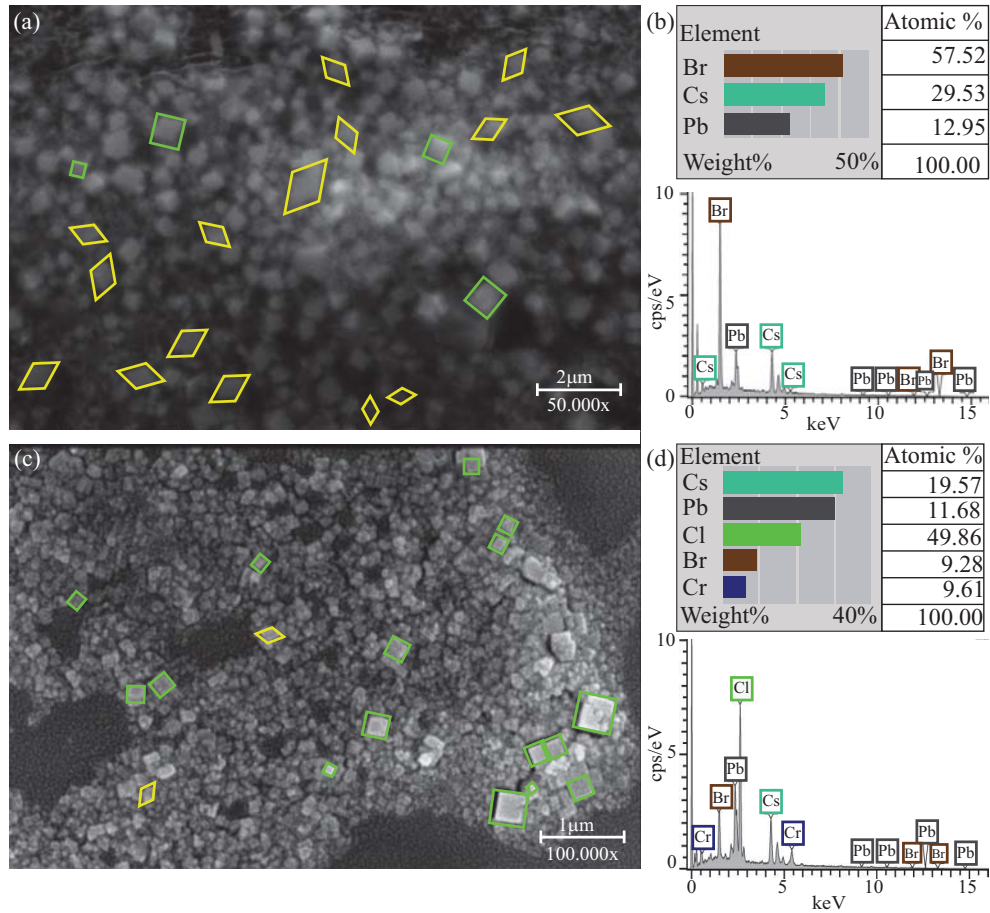
Figure 3.2. SEM images and energy dispersive X-ray (EDX) analysis of (a, c) Cr0, and (b, d) Cr75 samples.[108] Reprinted with permission from Ozen *et al.* J. Appl. Phys. 125(22):225705 2019. Copyright 2019 AIP Publishing.

To ensure the accuracy of the experimental findings and to see into the physics behind the dopant induced modifications, we analyzed neat and Cr-doped $CsPbBr_3$ and $CsPbCl_3$ crystal structures by using density functional theory-based calculations. The optimized lattice parameters are a=8.30 Å, b=7.93 Å, c=11.31 Å and a=7.93 Å, b=7.59 Å, c=10.83 Å for undoped orthorhombic (Pnma) $CsPbBr_3$ and $CsPbCl_3$ crystals, respectively. Besides, each Pb^{2+} atom bonds with six Br^- atoms with the 2.92 Å bond length in the $CsPbBr_3$ structure, while Pb-Cl bond length in the $CsPbCl_3$ is found to be 2.72 Å. Further, the Cr-doping scenarios are investigated by total energy calculations. Comparing total energies of neat and doped structures reveals 0.34 eV and 0.62 eV energy gain in the case of substitutional doping of Cr^{3+} atom as B-site cation into $CsPbBr_3$ and $CsPbCl_3$ host lattices, respectively. Very similar to the charge donation of the Pb^{2+} atom in the undoped

25

structure, Cr^{3+} donates 1 and 1.2 e to the $CsPbBr_3$ and $CsPbCl_3$ structures, respectively.
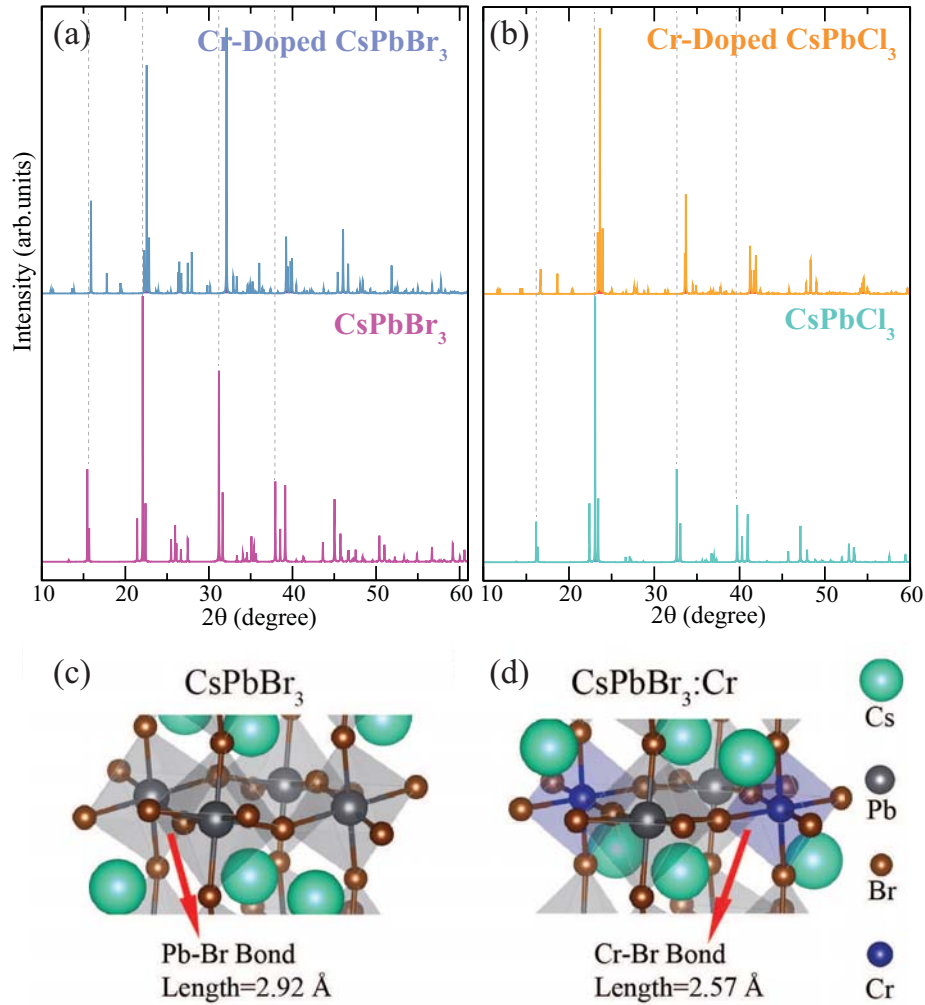
Figure 3.3. Calculated XRD patterns of bare and doped (a) $CsPbBr_3$, (b) $CsPbCl_3$ structures. Crystal structure of (c) undoped, (d) Cr-doped $CsPbBr_3$.[108] Reprinted with permission from Ozen *et al.* J. Appl. Phys. 125(22):225705 2019. Copyright 2019 AIP Publishing.

DFT calculations reveal that Pb-Cr substitution causes 6.77 % shrinkage in the host lattices of $CsPbBr_3$ structure and Cr-Br bond is 1.2 % shorter than the Pb-Br bond. Moreover, the characteristic XRD signals, marked with dashed lines, of bare $CsPbBr_3$ structure overlaps when theoretical and experimental X-ray diffractograms are compared. In the case of Cr-doping, a shift towards higher 2θ values in both experimental and theoretical X-ray diffractograms reveals the shrinkage originated from Cr-Pb substitutional doping.

3.1.2. CrCl$_3$-Driven Modifications in Electronic and Optical Properties

The Cr-doping process leads to modifications in the optical and electronic properties of perovskite crystal as well as structural changes. This subsection includes the results of optical measurements and electronic band dispersion calculations performed to understand these modifications.

PL spectra of Cr0, Cr25, Cr50, and Cr75 samples are presented in Fig. 3.4. Under 254 nm UV-light illumination, Cr0 sample exhibits sharp and single emission peak at 525 nm. However, unlike the undoped structure, Cr-doped samples exhibit additional distinctive PL peaks in the range of 400 - 775 nm. As shown in Fig. 3.4-(a), peaks in the different regions behave differently depending on the dopant ratio and are localized in the red, green, and blue region of the visible spectrum. Therefore, the PL spectrum is divided into three sections regarding these regions and clarified separately.
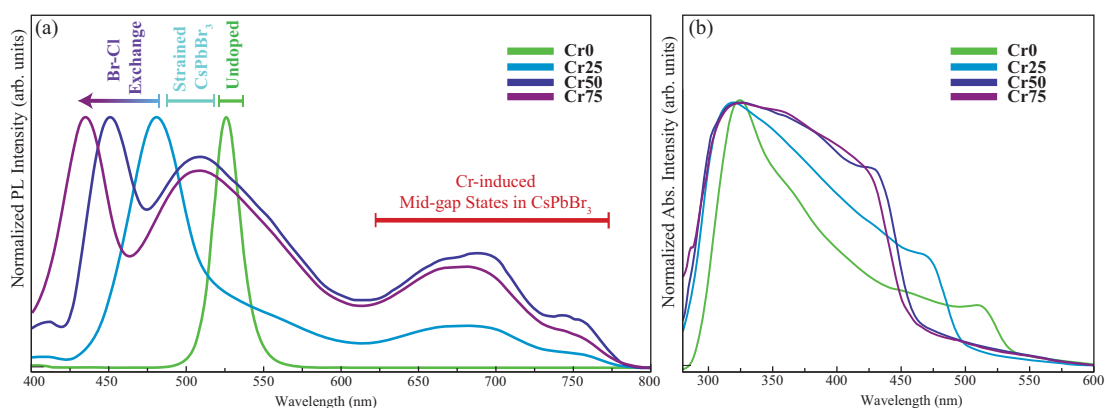
Figure 3.4. Normalized (a) PL, (b) absorption spectra of the Cr0, Cr25, Cr50, and Cr75 samples.[108] Reprinted with permission from Ozen *et al.* J. Appl. Phys. 125(22):225705 2019. Copyright 2019 AIP Publishing.

The first group in the blue region consists of three separately localized peaks between 476 and 427 nm. Although the blue shift in this region is proportional to the increase in the amount of the dopant solution, the origin of this shift is independent of the Cr^{3+} ratio. Peaks and such shifts in this region are originated from anion exchange.[54] Since increasing the amount of Cr by adding more CrCl$_3$ dopant solution also increases the amount of Cl$^-$ ions in the solution before crystallization. This increase enables more

27

anion (Br^--Cl^-) exchange and the number of Cl^- ions in the host lattice increases.

In the second group, peaks have emerged around 515 nm and behave differently than the first group. This group is completely independent of the amount of Cl^- ions. The XRD measurements and theoretical XRD calculations verify the shrinkage of the structure in the case of Cr-Pb substitution, while DFT based structural optimization calculations show that this substitution is energetically favorable. Besides, Pb-Cr substitution originated shrinkage of $CsPbBr_3$ structure have shown by DFT simulations. Due to this Cr-induced shrinkage in the structure, the bandgap of the host lattice increases and the emission peak shifts from 525 to 515 nm. The fact that this shift is independent of the amount of Cl^- indicating a barrier for anion exchange caused by the presence of Cr atoms in the $CsPbBr_3$ lattices.

The third group including broad emission peaks covers the large region between 675 and 775 nm. Similar to the second group, this region behaves independently from the amount of Cl^- ions and intensity of peaks increases related to the Cr^{3+} ratio. Electronic band dispersion calculations of undoped and doped $CsPbBr_3$ and $CsPbCl_3$ reveal the dopant-induced narrow and broad midgap states along the whole Brillouin Zone. Both experimental and theoretical results prove that, emission in this region originates from Cr-induced midgap states. These findings are the evidences of successful doping process as well as they explain the origin of the modifications.

Besides the PL spectrum, the absorption spectrum provides information about the optical and electronic properties of the materials. The normalized UV-Vis absorption spectra of the doped samples and undoped sample are presented in Fig. 3.4-(b). The effect of anion exchange is also seen in the absorption spectrum by the shift of the absorption edge from 530 through 460 nm.

On the other hand, the absorption spectrum of the neat sample exhibits two absorption peaks located at 235 and 525 nm, respectively. Intesities of these peaks are related with the formation of the different phases of cesium lead halide perovskite structures.[107,109] Absorption spectrum of Cr0 sample indicates the formation of Cs_4PbBr_6 with a trace amount of $CsPbBr_3$ crystals.

It is seen that the difference between the intensities of these peaks decreases by the increase in the dopant ratio. Compatible with the EDX, XRD, and SEM result, this change of the intensities indicates the dopant induced increase in the formation of $CsPbBr_3$ crys-

tals that are crystallized in a cubic shape. After the doping process, the form of absorption spectra begins to resemble the $CsPbBr_3$ NC absorption spectrum.[110]
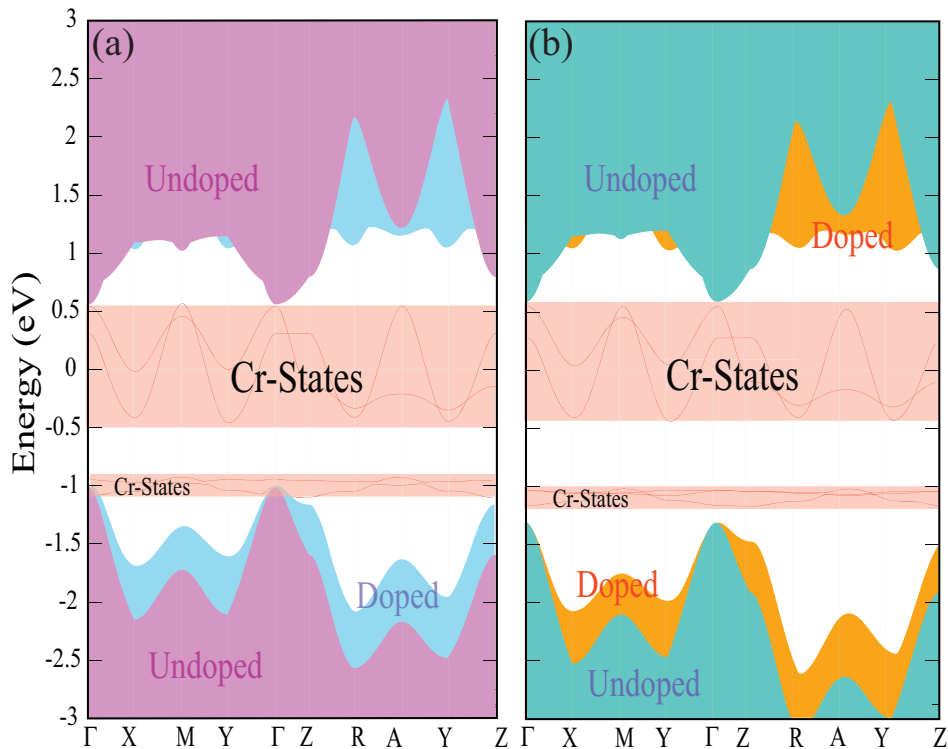
Figure 3.5. Electronic band dispersion of bare and doped (a) $CsPbBr_3$ and (b) $CsPbCr_3$ structures.[108] Reprinted with permission from Ozen *et al.* J. Appl. Phys. 125(22):225705 2019. Copyright 2019 AIP Publishing.

3.1.3. Single-Phase White Light Generation

The interaction of perovskites with air and moisture causes changes in the electronic structure and optical properties of perovskites. Although the Cr^{3+} doped perovskite nanocrystals initially emit violaceous light due to the high Cl^- ratio, the white light emission was observed after 30 days. This time-dependent shift was tracked by PL measurements and presented in Fig. 3.6. Comparing two measurements made at 30-day intervals, it was clearly seen that, intensity of PL peaks originated from anion exchange and strained $CsPbBr_3$ crystals decrease significantly and become comparable to the intensity of the PL peak originated from midgap states. Similar intensities of PL peaks at three region corre-

sponding to the RGB scale resulted in white light emission.
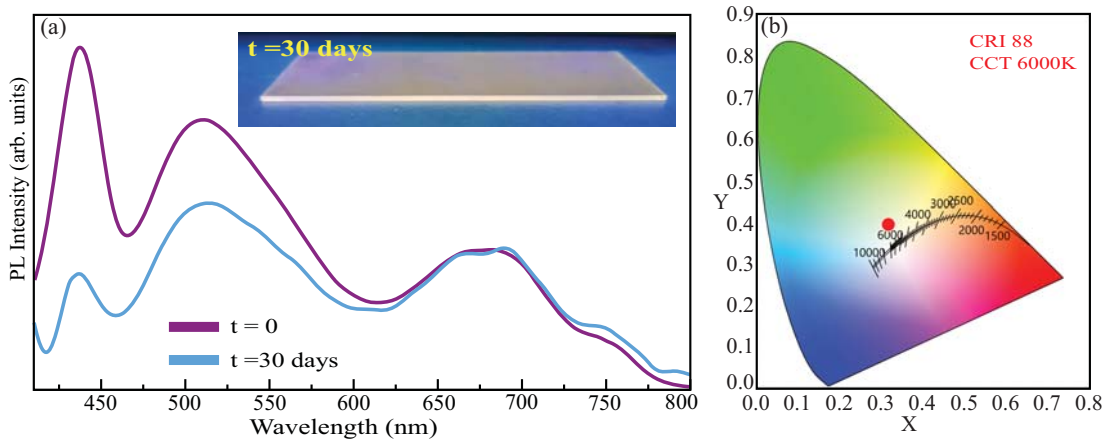
Figure 3.6. Photoluminescence spectrum of the Cr75 sample (a) at t = 0 and t = 30 days. Inset: the photographic image of the sample under 254 nm UV-light and (b) plotted on the CIE diagram at t = 30 days.[108] Reprinted with permission from Ozen *et al.* J. Appl. Phys. 125(22):225705 2019. Copyright 2019 AIP Publishing.

To understand the change in the intensities of the PL peaks, we performed DFT simulations to observe the effect of a water molecule on doped and neat $CsPbBr_3$ and neat $CsPbCl_3$ crystal structures. 150, 190, and 420 meV of adsorption energies per H_2O molecule were calculated for $CsPbBr_3$, $CsPbCl_3$, and Cr-doped $CsPbBr_3$, respectively. Obviously, the $CsPbCl_3$ crystals interact more strongly with the water while Cr-doped perovskite crystals interact weaker. This difference clarifies that moisture leads to more disruption of Cl-containing structures and a decrease in PL densities faster.

Commission Internationale de I′Eclairage (CIE) chromaticity diagram is used to characterize the colors. The red circle located at the color coordinates x = 0.3161 and y = 0.3938 confirms the generation of white light. These coordinates are quite close to the coordinates of pure white light ($x = y$ = 0.3333). Furthermore, this sample shows high Color Rendering Index (CRI) of 88 and Correlated Color Temperature (CCT) of 6000 °K indicating that it is commercially viable.

3.2. Increasing the Stability of CsPbI$_3$ Perovskites by Doping

In this section, procedures and results of heterovalent doping of cesium lead iodide perovskite crystals are presented. The neat and Gd^{3+} doped CsPbI$_3$ perovskite nanocrystals are synthesized at 150 °C using the hot injection method. Various amounts of dopants are used to understand the effects of the doping process on the nanocrystals. 0, 5, 10, and 15 % mole Gd^{3+} samples are labeled as neat, Gd5, Gd10, and Gd15, respectively. With the addition of Gd^{3+} ions to the host lattice, the stability of the α-CsPbI$_3$ perovskites in the ambient conditions is doubled compared to the undoped α-CsPbI3 perovskites. Moreover, by the intercalation of Gd^{3+} ions, photoluminescence quantum yield and fluorescence lifetime of α-CsPbI$_3$ perovskites increased 10 % and 35 % respectively. In addition, cohesive energies of neat and doped crystals are calculated by DFT based geometric optimization calculations. Lastly, the effects of dopants in the electronic band structure of the perovskite crystal are investigated and experimental findings are verified by using density functional theory.

Details about the chemicals and the synthesis of neat and doped CsPb$_x$Gd$_{1-x}$I$_3$ nanocrystals defined in subsections 2.1.1.1 and 2.1.1.3 respectively. Absorption, photoluminescence, photoluminescence quantum yield, and time-resolved lifetime measurements are carried out on a FS5 spectrofluorometer (Edinburg Instruments, U.K.)

For the DFT based calculations of neat and Gd doped CsPbI3 crystals, exchange-correlation potentials are approximated by using GGA[93] and the kinetic energy cutoff for plane-wave expansion was set to 250 eV. For the determination of accurate charge densities, Brillouin Zone integration was performed using Γ-centered k-point meshes of 3×3×3. Gaussian smearing of 0.1 eV was used for all structures. Comprehensive information about computational methodology is given in section 2.3.

3.2.1. Structural Analysis and Stability Increase

To confirm the doping process and to understand the structural modifications originated from the intercalation of various amounts of Gd^{3+} atoms into the host lattice of the CsPbI$_3$ structure, XRD measurements were performed and presented in Fig. 3.7. XRD reflections confirmed that all samples were synthesized in the pure cubic perovskite struc-

ture without any secondary phases. Also, the XRD reflections indicate the successful doping of Gd^{3+} atom to the structure. First, as the dopant ratio increases, the slight shift of the reflection signals to the higher 2θ values is observed. This shift is attributed to the Gd^{3+} - Pb^{2+} substitution. Since the ionic radius of the Gd^{3+} ($r_{Gd^{3+}} = 0.93$ Å) is smaller than the ionic radius of Pb^{2+} ($r_{Pb^{2+}} = 1.19$ Å), shrinkage in the structure and thus, shift in the XRD reflections are observed.
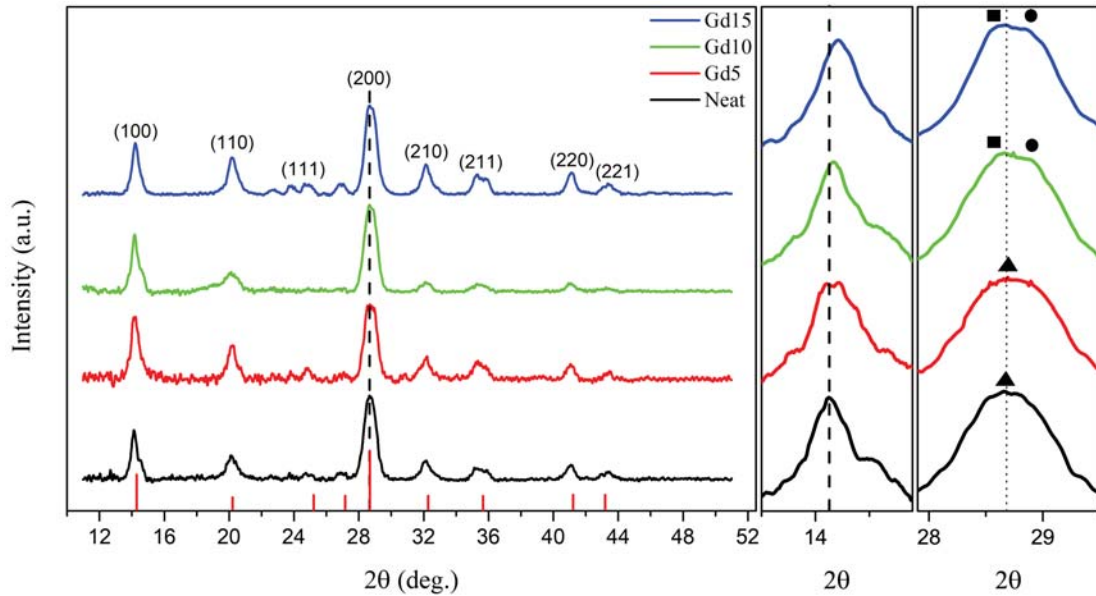
Figure 3.7. XRD patterns of neat, Gd5, Gd10, and Gd15 samples. Peaks shift at the (100) plane and peak splitting at the (200) plane.[111] Reprinted with permission from Guvenc *et al.* J. Phys. Chem. C 123(40):24865 2019. Copyright 2019 American Chemical Society.

Further, the dopant induced splitting in the XRD signal representing (200) plane shows that the dopant ions successfully takes place in the perovskite structure. This splitting is probably caused by reduced symmetry of the cubic phase by the intercalation of dopant ions. This kind of structural distortions can lead to an increase in the stability of the α-$CsPbI_3$. The peak splitting in (200) plane of Eu^{3+} doped $CsPbI_3$ structure is reported by Jane *et al.*.[51] The authors also mentioned that the distortion of the cubic structure increase the stability.

The stability and the distortion of the crystal structure can be indicated by using Goldschmidt's tolerance factor;

$$t = \frac{R_X + R_A}{\sqrt{2}(R_B + R_X)} \tag{3.1}$$

where R_X is the radius of the anion in the structure and R_A and R_B represent the radius of the A-site and B-site cations, respectively.[2,112,113] The effective radius of B-site cation (R'_B) is calculated by using;

$$R'_B = (1-x)R_{Pb^{2+}} + xR_{Gd^{3+}} \tag{3.2}$$

and the effective tolerance factor t' is calculated by using;

$$t' = \frac{R_X + R_A}{\sqrt{2}(R'_B + R_X)} \tag{3.3}$$

Since the ionic radius of Gd^{3+} is smaller than that of Pb^{2+}, Goldschmidt's tolerance factor increases in the case of Gd^{3+} incorporation into the host lattice. The tolerance factors for the neat, Gd5, Gd10, and Gd15 samples are calculated to be 0.807, 0.810, 0.813, and 0.817, respectively. This increase in the factor value indicates the dopant induced enhancement of stability.

Moreover, to understand the structural degradation and phase transitions we performed time-dependent XRD measurements for neat and Gd10 samples (Fig. 3.8). Characteristic reflection signals of the α-CsPbI$_3$ crystals observed in the neat sample have begun to disappear in 2 days and the complete phase transition to the δ-phase is observed in 5 days. Besides, for the Gd10 sample, the reflection signals indicating the presence of δ-phase were first observed on the 5th day and the complete transition to the δ-phase took 12 days after synthesis.

The structural analysis is completed by STEM imaging and comparison of particle size distributions of neat and Gd10 samples presented in Fig. 3.9. The neat sample has 15 $\pm$ 4 nm, while Gd10 exhibits 15 $\pm$ 2 nm of particle size distributions. It is observed that the length of the particles remains unchanged where the size distribution gets narrower after the doping process.
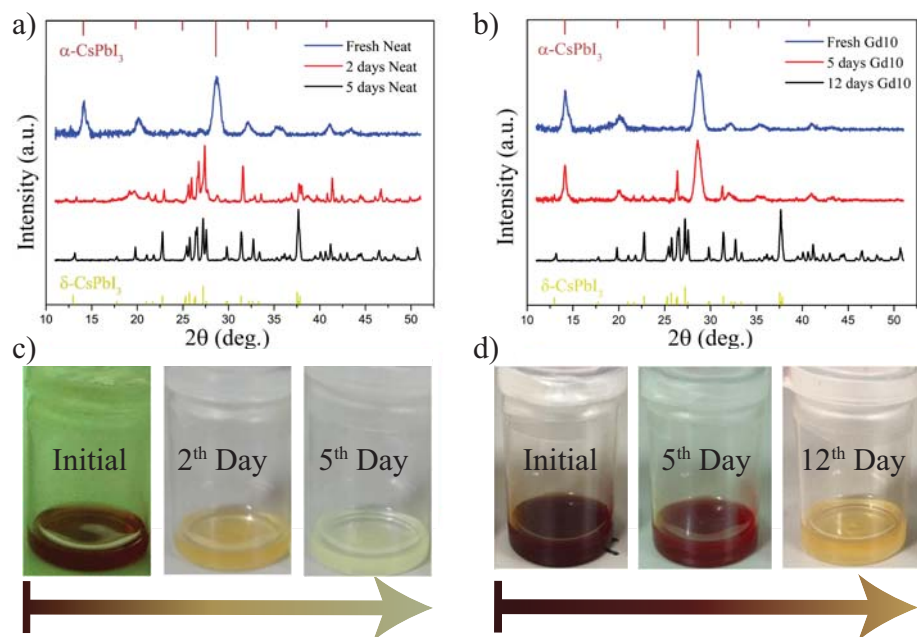
Figure 3.8. Time dependent XRD patterns and time-dependent images of (a, c) neat and (b, d) Gd10 samples.[111] Reprinted with permission from Guvenc *et al.* J. Phys. Chem. C 123(40):24865 2019. Copyright 2019 American Chemical Society.
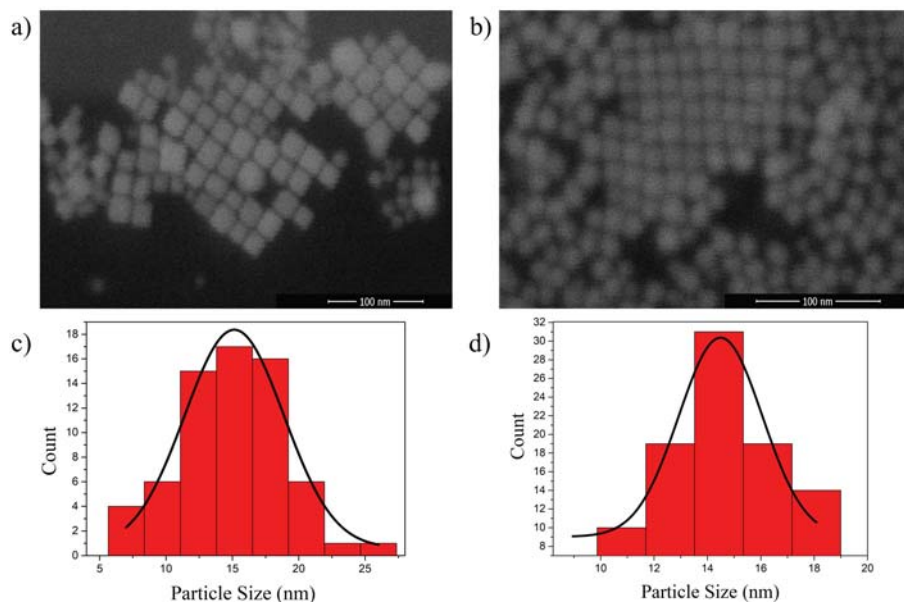
Figure 3.9. STEM images and particle distributions of (a, c) neat and (b, d) Gd10 samples.[111] Reprinted with permission from Guvenc *et al.* J. Phys. Chem. C 123(40):24865 2019. Copyright 2019 American Chemical Society.

3.2.2. Optical Analysis

To understand the Gd^{3+} induced modifications in the optical properties PL, absorption, PLQY, and lifetime measurements are carried out. (Fig. 3.10) The PL signal of the neat sample at 683 nm with 39.0 nm FWHM shows that our results are consistent with the literature.[18] All samples containing different amounts of Gd^{3+} exhibit nearly 1.8 eV direct bandgap. The corresponding PL peak positions of neat, Gd5, Gd10, and Gd15 samples are 683, 686, 688, and 683 nm, respectively. The red shift of Gd5 and Gd10 samples indicates the formation of dopant originated new states just below the conduction band.[114] On the other hand, contrary to this trend, although the increase in the dopant ratio, the blue shift was observed in the PL peak of the Gd15 sample. This shift can be attributed to the Moss-Burstein effect.[115,116] When excess n-type doping is applied on the host lattices of a semiconductor, the interaction between the dopants causes to partially filled impurity sub-bands occur within the conduction band. The possibility of this interaction is related to the amount of doping. When the extra electrons are introduced to the structure, Fermi level lies within the conduction band and higher levels of impurity sub-bands get occupied. This results in emission from higher states.

Moreover, PL FWHM values for neat, Gd5, Gd10, and Gd15 samples are 39.0, 34.5, 34.0, and 37.0 nm, respectively. The Gd10 sample has the narrowest FWHM among all samples. A trend similar to that of PL signals is observed in the view of FWHM values of the peaks. Since the more uniformly sized crystals obtained by doing up to the critical doping amount (10 % mole Gd^{3+}), the peaks get narrower. However, FWHM of Gd15 sample increases. This result is consistent with particle size distribution data obtained from STEM images.

The same trend continues in the PLQY measurement results consistent with previous measurements. 70, 74, 80, and 72% PLQY values recorded for neat, Gd5, Gd10, and Gd15, respectively. Obviously, Gd^{3+} doping increases the PLQY of the $CsPbI_3$ perovskite structure. This enhancement indicates the increased radiative transition amount induced by the defect reduction effect of Gd^{3+} ions. The reduction of defects attributed to the extra incorporation of I^- ions in the case of heterovalent doping.[46]
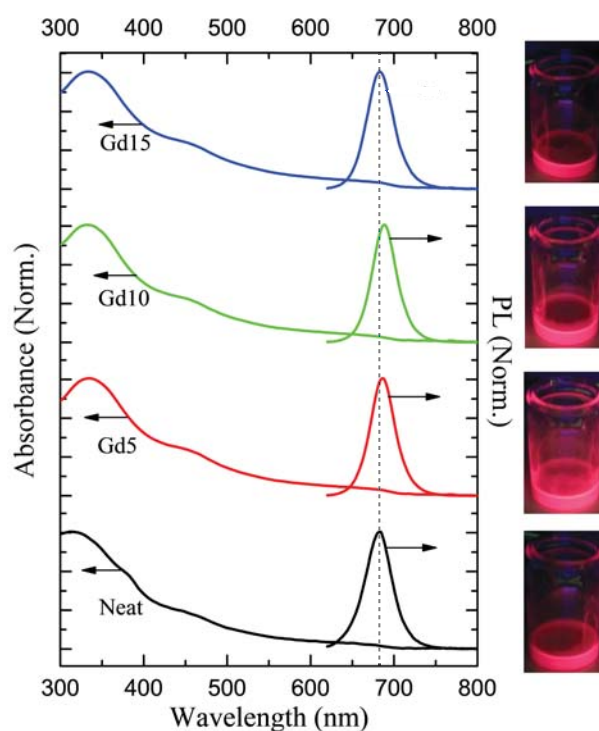
Figure 3.10. Absorption and PL spectra of neat and doped $CsPbI_3$ nanocrystals. Images of samples under 254 nm UV-illumination.[111] Reprinted with permission from Guvenc *et al.* J. Phys. Chem. C 123(40):24865 2019. Copyright 2019 American Chemical Society.

Sample	τ_1(ns)	τ_2(ns)	A_1(%)	A_2(%)	τ_{avg}(ns)
Neat	9.2	48.8	15.6	84.4	47.4
Gd5	15.6	60.2	19.8	80.2	57.5
Gd10	16.3	66.3	14.0	86.0	64.4
Gd15	11.4	34.3	33.6	66.4	31.0

Figure 3.11. (a) PLQYs of all samples excited with 460 nm wavelength light. (b) Time-resolved fluorescence lifetimes of all samples excited by 560 nm laser and collected lifetime decays fitted with the biexponential function. Inset: obtained data from fitted curves.[111] Reprinted with permission from Guvenc *et al.* J. Phys. Chem. C 123(40):24865 2019. Copyright 2019 American Chemical Society.

For further investigation, time-resolved fluorescence lifetime measurements were performed. Fluorescence lifetime curves were fitted with the biexponential function to calculate slow (radiative recombination) and fast (non-radiative recombination) components. Fluorescence lifetime curves and data set obtained from fluorescence lifetime curves are shown in inset of Fig. 3.11-(b). The average lifetime was calculated using the following equation;

$$t_{avg} = \frac{A_1 \tau_1^2 + A_2 \tau_2^2}{A_1 \tau_1 + A_2 \tau_2} \tag{3.4}$$

where A_1 and A_2 are the constants and τ_1 and τ_2 are the fast and slow recombination times, respectively.

For the Gd10 sample, the radiative component value increases from 48.8 to 66.3 ns while the calculated average lifetime increases from 47.4 ns to 64.4 ns. As expected both the radiative component and the calculated average lifetime decreases for the Gd15 sample. It is clear that Gd^{3+} doping up to a certain point increases the contribution of the radiative component and prolongs the average lifetime. Similarly, an increase in the radiative component of the lifetime and its contribution to the average lifetime by doping is reported. This enhancement may be originated from reduced defects that are generated again in the case of high doping levels.
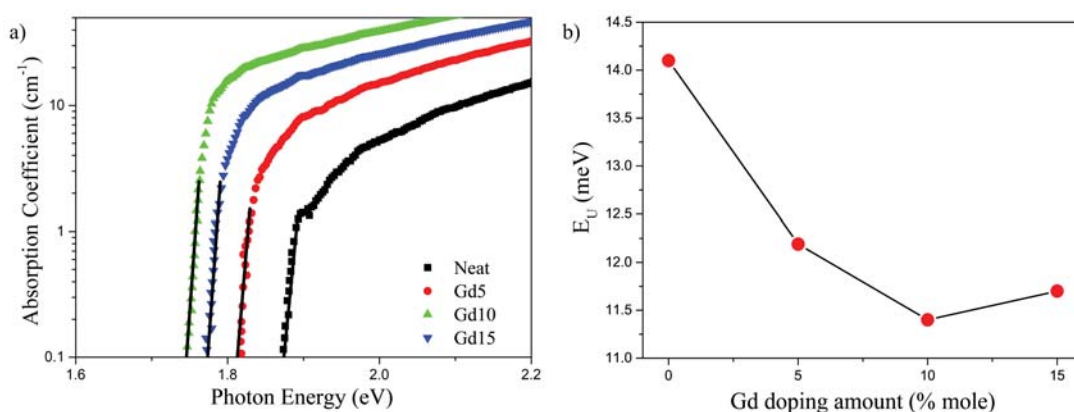
Figure 3.12. (a) Absorption coefficients on log scale and (b) Urbach energies of neat and doped samples.[111] Reprinted with permission from Guvenc *et al.* J. Phys. Chem. C 123(40):24865 2019. Copyright 2019 American Chemical Society.

In the absorption spectra of undoped and doped samples, a sharp excitonic signal

indicating the presence of nanowires or nanoplatelets is not observed.[117,118] Consistent with STEM images, absorption edges indicating the formation of nanocubes were observed. Further investigation on structural properties and stability is performed by calculating the Urbach energies. Structural disorder and imperfections result in localized states near the optical band edge. Therefore, a large exponential part appears along the absorption coefficient curve of low crystalline, disordered, and amorphous structures. This curve is also called the Urbach tail.[119] To examine and compare the Urbach tails of samples, their absorption coefficient versus photon energy graphs were plotted. The logarithmic part of the absorption coefficient is fitted using Urbach's rule;

$$\alpha(E) = \alpha_0 \exp\left[\sigma(T)\frac{(E - E_0)}{k_B T}\right] \tag{3.5}$$

where $\alpha(E)$ is the absorption coefficient; E, E_0, and α_0 are the characteristic parameters of the material; $\sigma(T)$ is the steepness factor; k_B is the Boltzman constant; T is the absolute temperature.

Urbach tails and Urbach energies that are calculated by using the slope of fit given in Eq. 3.5 are presented in Fig. 3.12. Urbach energy and structural disorder are inversely proportional. The Urbach energy of the neat sample is calculated to be 14.1 meV. By incorporation of the Gd^{3+} ion to the sys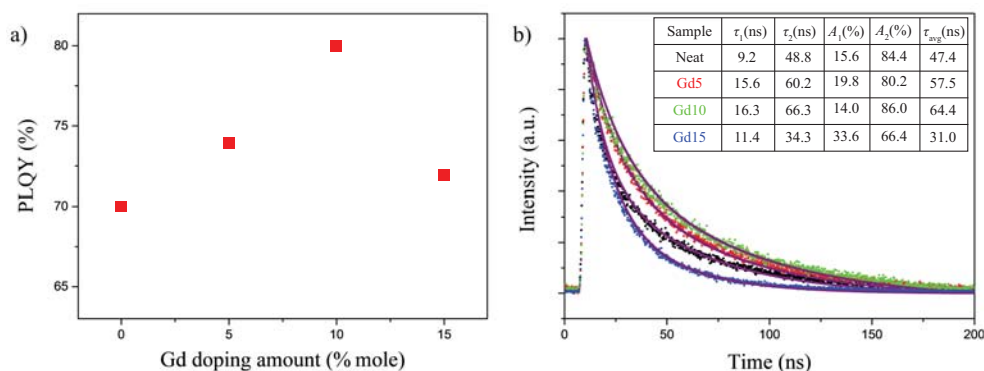tem, Urbach energy of Gd5 sample decreases to 12.19 meV. With the increase in the dopant ratio, the Urbach energy, decreases to 11.4 meV for the Gd10 sample. However, in the case of excessive doping, the Urbach energy of the Gd15 sample increased to 11.7 meV. This trend obviously shows that Gd^{3+} doping decreases the defect density. Besides, the increased the Urbach energy of the Gd15 sample indicates the over-doping promoted trap defects. A similar trend in the Sb^{3+} doped $CsPbBr_3$ perovskite has been reported by Zhang *et al.*.[53] Authors showed that heterovalent doping causes a decrease in the defects up to a certain point, and when this point has exceeded the increase in the number of defects is inevitable. Also the trend observed in Urbach energies is consistent with the results of photoluminescence, lifetime, and PLQY measurement.

3.2.3. Theoretical Analysis

The energy optimization calculations and the electronic band dispersions of neat and Gd^{3+} doped structures are performed by using DFT calculations. The cohesive energies per atom for neat and doped structures are found to be 3.32 and 3.22 eV, respectively. The formation of Gd^{3+} doped $CsPbI_3$ perovskite is 0.1 eV more favorable when the Gd^{3+} ions included before the crystallization.

Each Gd^{3+} ion donates 0.12 eV more charge than Pb atoms in the case of Gd^{3+}-Pb^{2+} substitution. Donated charge amounts per atom are found to be 0.76 and 0.64 eV for Gd^{3+} and Pb^{2+} ions, respectively. Therefore, the extra charge around the Gd^{3+} ion, 7.52% shortens the lengths of Gd - I bonds (3.19 Å) that form the $[GdI_6]^{-4}$ octahedra compared to the Pb-I bonds (2.95 Å) forming $[PbI_6]^{-4}$ octahedra. This shrinkage is consistent with the slight shift on the theoretical XRD calculations and experimental XRD measurements. Finally, electronic band dispersions reveal that Gd-Pb substitutional doping is n-type doping that changes the electronic properties of the $CsPbI_3$ structure.
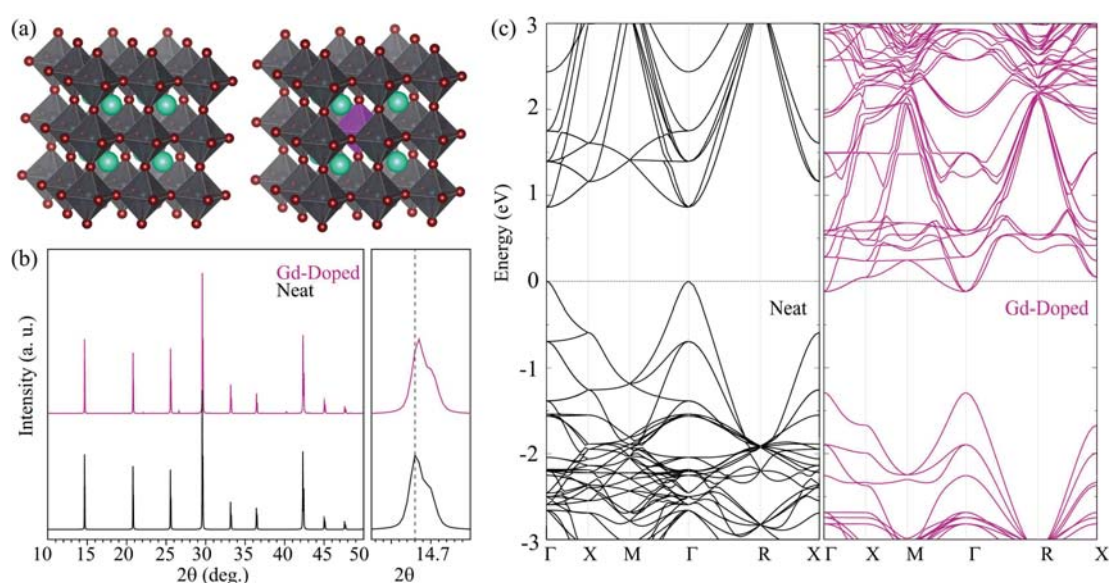
Figure 3.13. (a) Structures, (b) calculated XRD patterns, and (c) electronic band dispersion diagrams of neat and Gd^{3+} doped $CsPbI_3$ structures.[111] Reprinted with permission from Guvenc *et al.* J. Phys. Chem. C 123(40):24865 2019. Copyright 2019 American Chemical Society.

CHAPTER 4

FUNCTIONALIZATION OF CESIUM LEAD HALIDE PEROVSKITES BY DIMENSIONAL MODIFICATIONS

In the last decade, their outstanding properties such as tunability, narrow full width half maximum (FWHM) emission peak, high PLQY, large absorption spectrum, high defect tolerance, long carrier lifetime, and high charge carrier density make perovskites a promising class of semiconductors.[18, 19, 20, 21, 22, 55, 98, 99, 100] Over time, investigative efforts have turned to the use of perovskites in optoelectronic devices such as LEDs, photodetectors, lasers, solar cells.[80, 120, 121, 122, 123, 124]

Scientists have developed many different synthesis methods in the search of functionalization of perovskites to use them in optoelectronic devices. For this purpose, many different sizes of perovskites, from quantum dots to single-crystal structures, were synthesized and used in device fabrication.[125, 126, 127, 128, 129, 130, 131]

However, certain problems have arisen with the use of different sizes of perovskites in optoelectronic devices. In large structures containing many grain boundaries, electroluminescence (EL) efficiency of perovskite LEDs (PeLEDs) decreases due to the increase in the non-radiative transitions originated from trap states.[132, 133, 134, 135, 136] Also, this trap state-induced nonradiative transitions decrease the quantum yield and the lifetime.[137] Therefore, to use them in optoelectronics, synthesis and fabrication of low dimensional, defect tolerant inorganic lead halide perovskites with controllable size, morphology, and composition is inevitable.[138]

Another obstacle before achieving desired properties is the coating process that may cause inhomogeneity and decrease in the efficiency. To overcome this issue and reduce to required steps for perovskite synthesis and device fabrication, single-step strategies such as chemical vapor deposition, antisolvent vapor treatment, spray coating, and electrospraying have been developed.[139, 140, 141, 142, 143, 144]

On the other hand, the emission peak in the red zone and the low band energy range of 1.7 eV made the $CsPbI_3$ perovskite structure stand out among other cesium lead halide perovskites. Motivated by its desirable bandgap energy, many scientists worked on the basic properties of this material to completely understand its crystal structure,

possible phases, optical, and electronic properties. Its optical properties make this material remarkable for many device technologies, such as photovoltaic cells, light-emitting diodes, and photodetectors. However, although the emissive black phase is stable at high temperatures, its transition into a non-radiative and non-perovskite yellow phase at room temperature is a major obstacle for the advances in this area. No matter how much the efficiency of $CsPbI_3$ perovskite crystals goes, it seems impossible to make them suitable for commercial use without obviating the instability issue.

Therefore, a great deal of work on $CsPbI_3$ perovskite structures is focused on solving the stability issue. Different strategies such as doping, ligand modifications, and thickness modifications are used to increase the stability of $CsPbI_3$ perovskites, prevent or retard the phase transition enough to use in devices. On the other hand, there is an orthorhombic phase between $CsPbI_3$ perovskites, which is more stable than cubic α-$CsPbI_3$ at room temperature.[145, 146] Understanding this phase may be one of the main steps to make $CsPbI_3$ perovskites suitable for use in optoelectronic devices. However, there are very few studies examining the changes in the properties of $CsPbI_3$ depending on their thickness.

4.1. Tuning the Optical Properties of $CsPbBr_3$ Perovskites by Dimensional Modifications

In this chapter, the dimensional dependency of structural, optical, electronic, and vibrational properties of cesium lead bromide perovskite structure and facile synthesis method are investigated. The $CsPbBr_3$ perovskite nanoplatelets are synthesized by using the electrospraying technique with the innovative use of the known experimental setup. The single-step process is reported for the $CsPbBr_3$ nanoplatelet synthesis and surface coating. Additionally, to understand the effects of experimental parameters on optical properties and crystal structure of $CsPbBr_3$ perovskite nanoplatelets, a comprehensive experimental study is performed on the characterization of the molar ratio of surfactants (OA, OLAM), the magnitude of the electric field, syringe-sample distance, and the flow rate. Moreover, we tuned the optical properties of $CsPbBr_3$ nanoplatelets by the ligand ratio mediated dimensional modifications.

4.1.1. Experimental Setup and Characterization
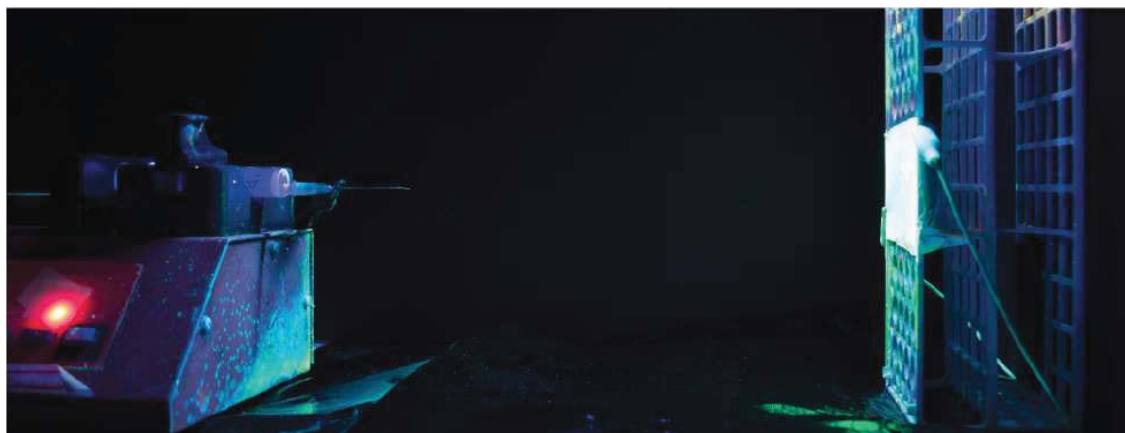
Figure 4.1. Photographic image of electrospraying setup.[147] Reprinted with permission from Ozcan *et al.* ACS Appl. Nano Mater C 2(8):5149 2019. Copyright 2019 American Chemical Society.

The electrospraying setup includes, syringe pump, power supply, syringe, and ITO coated glass as a substrate. The electrospraying method is mainly based on antisolvent evaporation. Plastic syringe is loaded with a 0.4 mL precursor solution and placed on to programmable syringe pump. DC voltage in the magnitude of kV is applied to the needle tip while the substrate is grounded to create potential. Under the electric field created between the needle and the substrate, the pump pushes the precursor solution out of the syringe and the electric field directs the precursor droplets containing dissolved salts and surfactants to the grounded substrate. As the accelerated DMF evaporates, the droplet's solubility decreases and salts and ligands come together to form perovskite on the substrate. During this process, there are different parameters that can affect the crystallization, such as flow rate, needle tip-substrate distance, and magnitude of the magnetic field.

To understand the effect of physical parameters on crystallization, several characterization attempts are made using the precursor solution recipe reported by Li *et al.*.[86] At the first set electrospraying is performed with flow rates of 0.25, 1.00, and 1.50 mL/hr and the time to spray 0.4 mL of the precursor solution was recorded as 96, 24 and 16 minutes, respectively. In the case of 0.25 mL/hr flow rate, the low PL intensity at higher energies

is originated from exposure of crystals to ambient conditions for a longer time and less evaporation of antisolvent. In the second set, applied voltage is set to the 10, 15, and 20 kV by using 1.5 mL/hr flow rate. Since the potential difference controls the speed of the droplets, it is obvious that the 10 and 15 kV potential difference is not sufficient for the evaporation. The desired amount of evaporation for the crystallization is obtained by 20 kV potential difference. Lastly, the distance between the needle tip and the substrate was characterized by trials of 10, 16, and 23 cm distances. While it was seen that 16 cm was not sufficient for evaporation of the precursor solution, it was understood that the distance of 30 cm was too far for the spraying process. After the characterization trials, flow rate, applied voltage, and distance are specified as 1,5 mL/hr, 20 kV, and 16 cm, respectively.
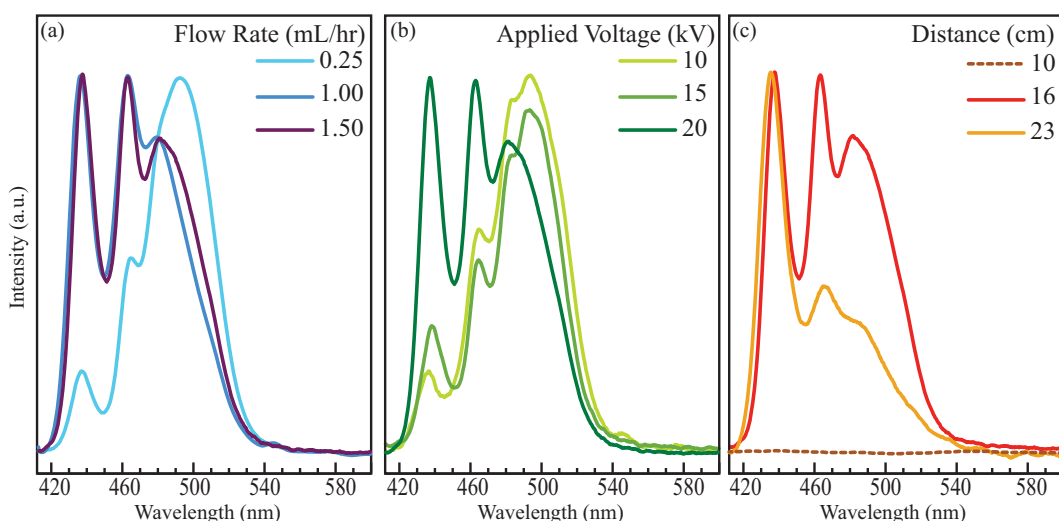
Figure 4.2. PL spectra of control sample under various (a) flow rates, (b) applied voltages, and (c) distances.[147] Reprinted with permission from Ozcan *et al.* ACS Appl. Nano Mater C 2(8):5149 2019. Copyright 2019 American Chemical Society.

4.1.2. Ligand Ratio Mediated Thickness Control

In order to identify the thickness dependent optical properties of electrosprayed perovskites, the characterized synthesis method was performed by using 500 μL of OA and various amounts of OLAM. Since the OLAM molecules cover to the surface of the perovskite crystals, they act as an intercalating agent and creates a barrier against inte-

gration. Their appearance and emission color under UV illumination is presented in Fig. 4.3.
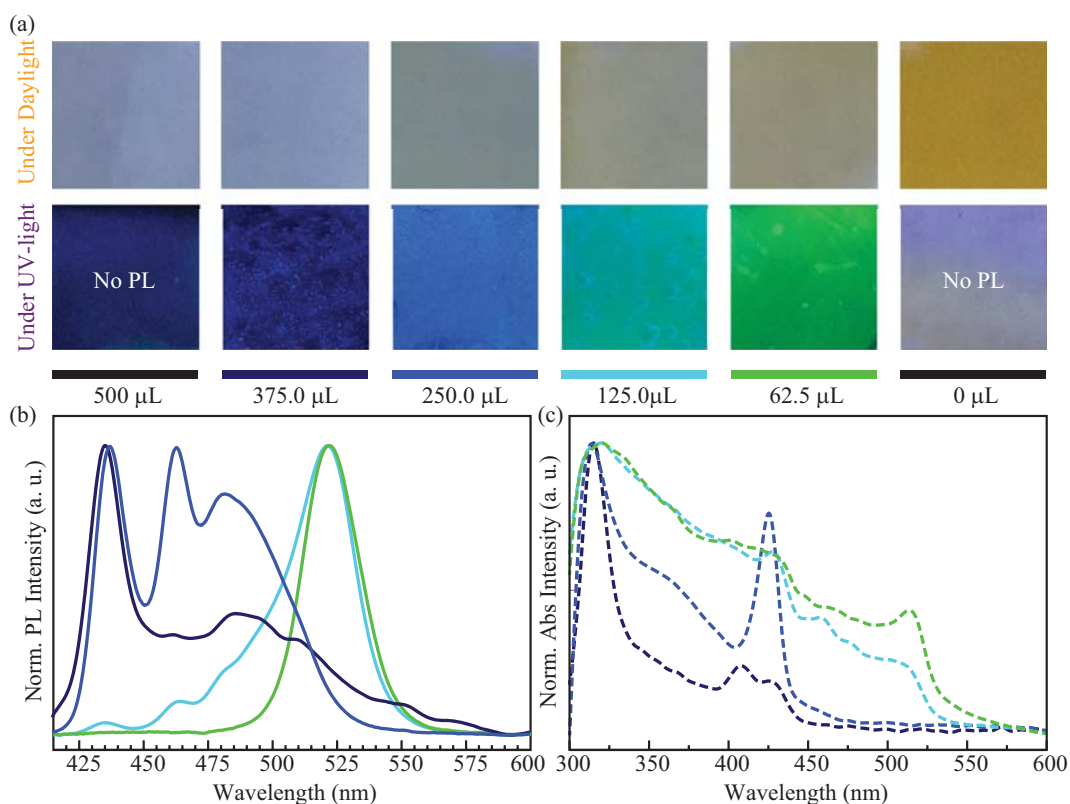
Figure 4.3. (a) Photographic images, (b) photoluminescence, and (c) absorption spectra of perovskite films with varying amount of OAm and 500 μL oleic acid.[147] Reprinted with permission from Ozcan *et al.* ACS Appl. Nano Mater C 2(8):5149 2019. Copyright 2019 American Chemical Society.

By the increase in the OLAM, emission color of perovskite crystals is tuned from green towards dark blue. The decrease in the amount of OLAM causes larger and more defect-containing crystals to form.[148] Besides, the excessive use of OLAM passivates the crystallization and changes the phase of the formed crystals. Therefore, in the absence of OLAM and in the case of its excessive use, no emission is observed. On the other hand, significant changes are observed in PL spectrum of perovskites depending on the amount of OLAM. The sample with 375 μL OLAM exhibits one sharp (440 nm) and less intense broad peaks in the region between 460 - 560 nm. OLAM acts as intercalating agent and plays an important role in the formation of ultru-thin nanoplatelets. As the amount of OLAM decreases to the 250 μL, intensity of broad peaks increase. This change

in the PL spectrum of the samples indicates that by the decrease in the surfactant ratio, nanoplatelets coalesce with nearby counterparts. This coalesce results in formation of thicker nanoplatelets. By decreasing the OLAM ratio to 125 and then 62.5 μL, green emitting nanoplatelets with a single PL peak around 525 nm is obtained. This quantum confinement effect is clearly shown in Fig. 4.3.[76, 149]

STEM images of blue, cyan, and green emitting samples are taken to understand the structural modifications arise from the differences in the OLAM ratio. To perform STEM characterization, the samples are dispersed in the hexane and the colloidal dispersion in hexane was drop-casted on Formvar reinforced copper grids and dried under a vacuum. Regional contrast differences indicate the vertically stacked nanoplatelets.

Further structural analysis of the nanoplatelets were performed by XRD measurements. The 2θ reflections at 15 ° and 30 ° refer to (001) and (002) planes, respectively (JPDCS no. 01-075-0412). The reflection signals of green emitting and non-emissive samples match well with the cubic phase of $CsPbBr_3$. However, as the OLAM increases, these signals disappeared and the new signals that hint about the presence of perovskite nanoplatelet have emerged.[149, 73]
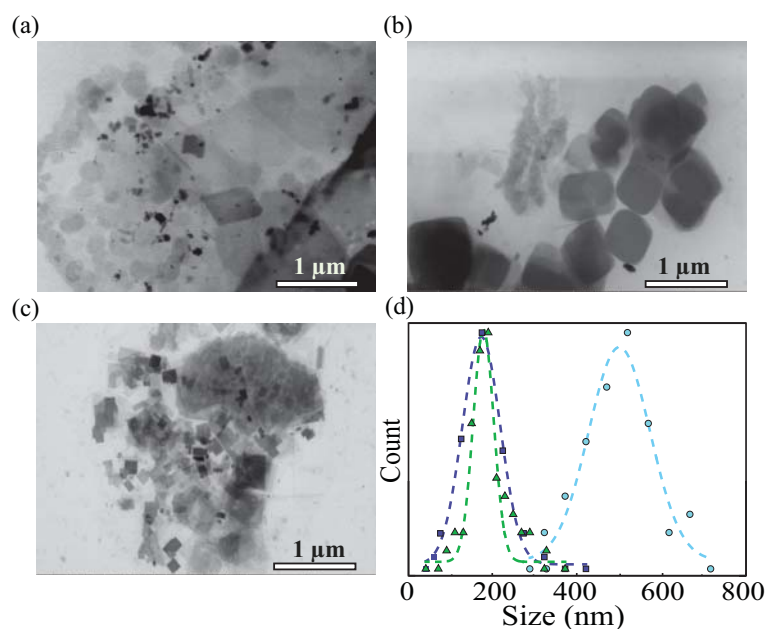
Figure 4.4. STEM images of (a) blue-, (b) cyan-, (c) green emitting perovskite films on ITO coated glass, and (d) particle size distributions.[147] Reprinted with permission from Ozcan *et al.* ACS Appl. Nano Mater C 2(8):5149 2019. Copyright 2019 American Chemical Society.
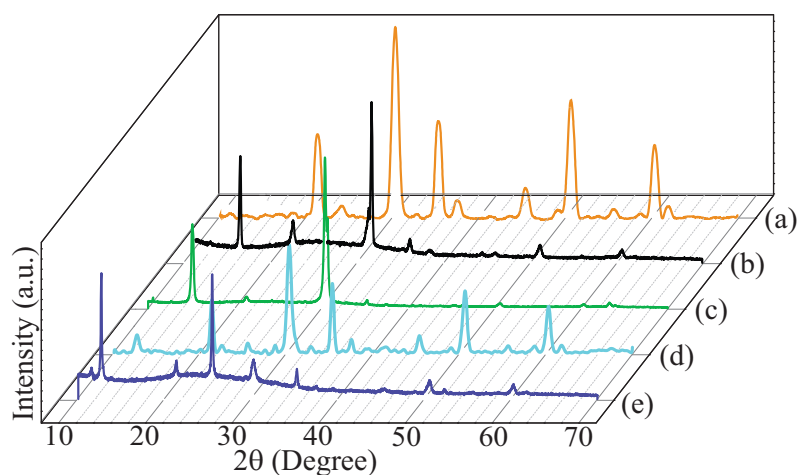
Figure 4.5. XRD reflection patterns of (a) ITO coated glass substrate, (b) non-emissive, (c) green emitting, (d) cyan emitting, and (e) blue emitting perovskite films on ITO coated glass.[147] Reprinted with permission from Ozcan *et al.* ACS Appl. Nano Mater C 2(8):5149 2019. Copyright 2019 American Chemical Society.
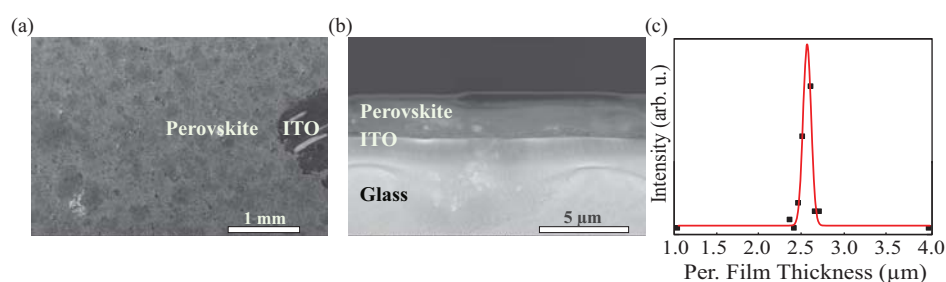
Figure 4.6. (a) Surface, (b) cross-section SEM images, and (c) thickness distribution of perovskite films on ITO coated glass substrate.[147] Reprinted with permission from Ozcan *et al.* ACS Appl. Nano Mater C 2(8):5149 2019. Copyright 2019 American Chemical Society.

The investigation of morphology and thickness are performed by surface and cross-section SEM images presented in Fig. 4.6. When the cross-section SEM image and the thickness of the film are considered, 2.5 μm thickness distribution proves the ability of electrospraying technique to be used in optoelectronic device fabrication processes.

4.1.3. Coating

One of the most important points in optoelectronic device fabrication is to cover the desired material on the surface in the desired pattern without any change in the material's properties. With a proper coating method, it is possible to make heterostructure or circuit designs. Here we used polyethylene terephthalate (PET) made mask to cover the ITO substrate with a IZTECH logo consists of perovskite. That logo proves that electrospraying is an efficient way of not only synthesis but also the coating process which is crucial for optoelectronic devices.
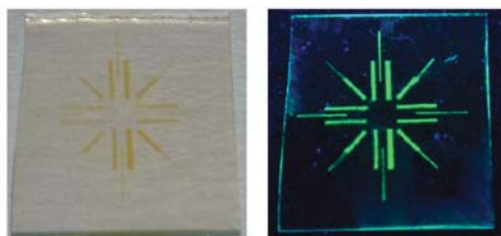
Figure 4.7. Electrosprayed perovskite IZTECH logo under daylight and UV-light.[147] Reprinted with permission from Ozcan *et al.* ACS Appl. Nano Mater C 2(8):5149 2019. Copyright 2019 American Chemical Society.

4.2. Tuning the Properties of CsPbI$_3$ Perovskites by Dimensional Modifications

In this section, the dimensional dependency of structural, optical, electronic, and vibrational properties of synthesized orthorhombic cesium lead iodide perovskite structures are presented.[145, 146] The possible bilayer and monolayer structures of bulk CsPbI$_3$ crystal structure are constructed and investigated on the basis of density functional theory in detail. It is shown that bilayer and monolayer forms with Cs-I terminated surfaces and bulk structure are dynamically stable among predicted two bilayer and three monolayer forms of orthorhombic CsPbI$_3$ perovskite crystal. In addition, the electronic properties of dynamically stable structures are investigated by electronic band dispersion calcula-

tions (LDA+PBE0+SOC), while the thermal stability of the encapsulated monolayer is investigated by molecular dynamics simulations.

The DFT based calculations of bulk $CsPbI_3$ structure and its bilayer and monolayer forms, exchange-correlation potentials are approximated by using LDA[94] and the kinetic energy cutoff for plane-wave expansion is set to 500 eV. For the determination of accurate charge densities, Brillouin Zone integration was performed using Γ-centered k-point meshes of 4×4×3, 4×4×1, and 4×4×1 for bulk, bilayer, and monolayer structures respectively. For bulk structure 0.1 eV, for bilayer and monolayer structures 0.05 eV Gaussian smearing is used. The charge donated and received by atoms is calculated by using Bader technique.[96] The stability of the structures against temperature is examined *ab-initio* molecular dynamics (MD) simulations. Additionally, phonon band dispersions are calculated by using the PHONOPY code to investigate the dynamical stability.[97] Comprehensive information about computational methodology is given in section 2.3.

4.2.1. Bulk Orthorhombic CsPbI$_3$

First, to fully characterize the bulk orthorhombic $CsPbI_3$ energy optimization calculations are performed. Fig. 4.8 shows the side and top view of the crystal structure with tilted $[PbI_6]^{-4}$ octahedrals compared to the cubic phase. The *a*, *b*, and *c* lattice parameters are found to be 7.93 Å, 8.94 Å, and 12.21 Å, respectively. According to Bader charge analysis, the charges donated by Cs and Pb atoms are 0.78 and 0.81 *e*, respectively. The charge received by each I atom is 0.53 *e*.

To investigate the dynamical stability of bulk orthorhombic $CsPbI_3$ structure, the small-displacement methodology is used to obtain elements of the dynamical matrix and corresponding phonon spectrum. The phonon spectrum of the bulk $CsPbI_3$ crystal exhibits real eigenvalues through all the symmetry points, confirming the dynamical stability of the structure and the reliability of the computational methodology.

Electronic band dispersion of the bulk structure presents a 1.9 eV direct bandgap. It is known that around the band edges, the contribution of the Cs atom is negligible.[84] The VBM and CBM of the bulk structure possesses at Γ point and dominated by I-*p* and Pb-*p* orbitals.
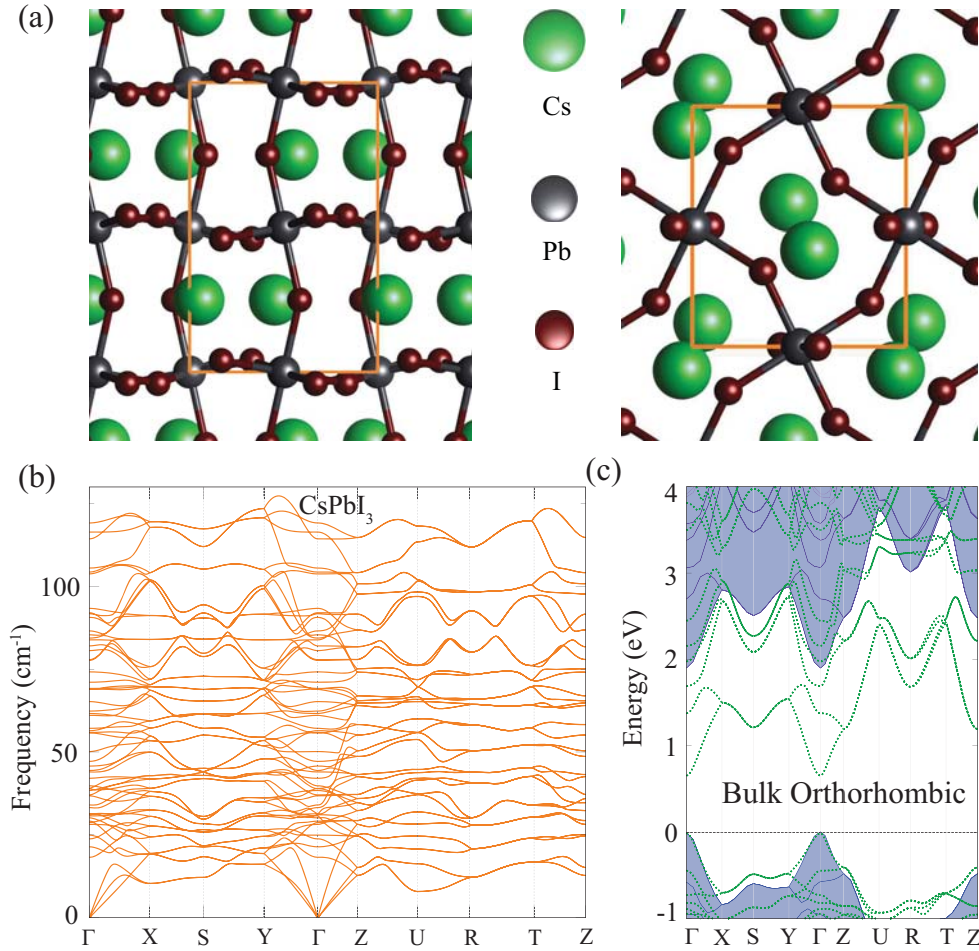
Figure 4.8. Bulk CsPbI$_3$: (a) side view, (b) top view, (c) phonon band diagram, and (d) electronic band dispersion.[150] Reprinted with permission from Ozen *et al.* Comput. Condens. Mater. 23:e00453 2020. Copyright 2020 Elsevier B. V.

4.2.2. Possible Bilayers of Orthorhombic CsPbI$_3$

To figure out the thickness-dependent properties, two bilayer structures are derived from the bulk CsPbI$_3$ regard to the atoms on their surfaces. The structure that has the Cs and I atoms at the surface is given by the chemical formula Cs$_3$Pb$_2$I$_7$, while Cs$_2$Pb$_3$I$_8$ is used for the structure with a surface composed of Pb and I atoms.

Among possible bilayer structures, Cs$_2$Pb$_3$I$_8$ is dynamically unstable as can be seen from the imaginary eigenvalues possessing from Γ to S in Fig. 4.9. Besides, dynamically stable Cs$_3$Pb$_2$I$_7$ exhibits real eigenvalues through all the symmetry points. The optimized lattice parameters are found to be a = 7.62 Å and b = 9.16 Å for Cs$_3$Pb$_2$I$_7$

bilayer with a thickness of 12.46 Å. The cohesive energy per atom of the stable mono-layer is found to be 3.13 eV. The fact that the $Cs_3Pb_2I_7$ structure has formation energy close to that of the bulk structure (3.40 eV) and exhibits real eigenvalues in the phonon dispersion band diagram indicating the possibility of the stable ultra-thin structure of the orthorhombic $CsPbI_3$.

Due to the Bader charge analysis, Pb and Cs atoms donate 0.75 and 0.78 *e* charge. In response to this, 0.6 *e* and 0.5 *e* charge are received by surface and inner I atoms, respectively. Although thinning the structure causes the origin of unbonded atoms on the surface, $Cs_3Pb_2I_7$ exhibits a direct bandgap of 2.6 eV. Similar to the bulk structure, the VBM and CBM possess at Γ, but the dimensional modification increases the bandgap of the monolayer structure about 0.7 eV.
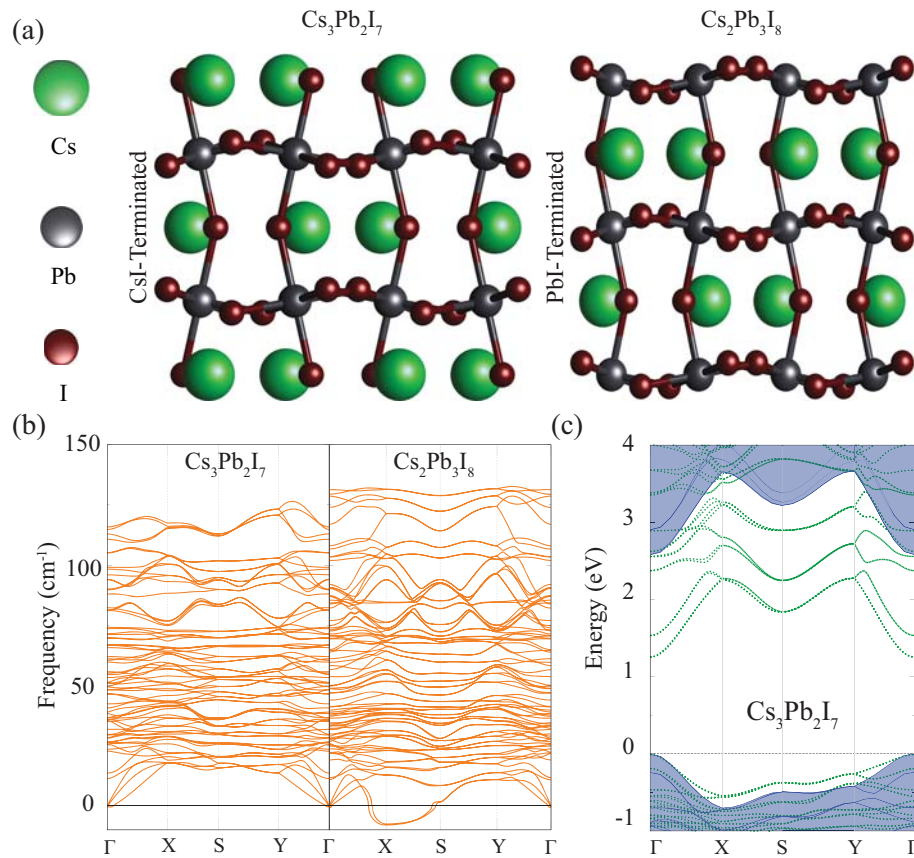
Figure 4.9. Possible bilayers of $CsPbI_3$: (a) side views, (b) phonon band dispersions of $Cs_3Pb_2I_7$ and $Cs_2Pb_3I_8$, and (c) electronic band dispersion of $Cs_3Pb_2I_7$.[150] Reprinted with permission from Ozen *et al.* Comput. Condens. Mater. 23:e00453 2020. Copyright 2020 Elsevier B. V.

4.2.3. Possible Monolayers of Orthorhombic CsPbI$_3$

To complete the analysis of thickness-dependent modifications on the CsPbI$_3$ structure, we constructed three possible monolayer forms of the bulk structure. Regarding atomic compositions, these monolayers are named as CsPb$_2$I$_5$, CsPbI$_4$, and Cs$_2$PbI$_4$. Phonon calculations reveal that the Cs-rich Cs$_2$PbI$_4$ form is the thinnest, dynamically stable monolayer form of CsPbI$_3$. The cohesive energy per atom for Cs$_2$PbI$_4$ is found to be 3.08 eV. The dimensional reduction leads to a decrease in the *a* and increase in the *b* lattice parameters, respectively. The lattice parameters of dynamically stable thinnest form are found to be $a = 7.38$ Å and $b = 9.28$ Å with the thickness of 6.30 Å.
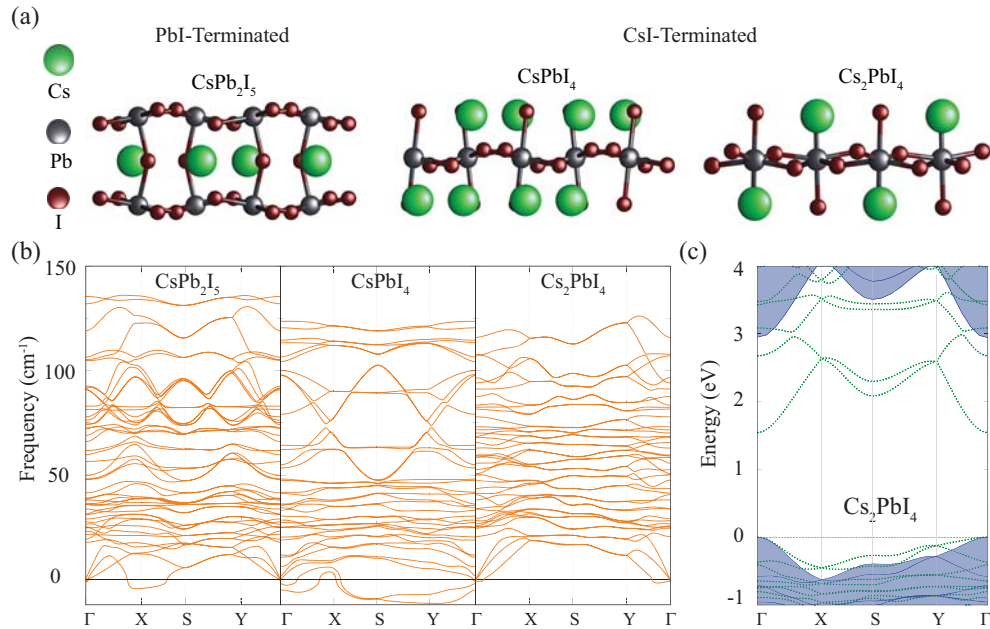
Figure 4.10. Possible monolayers of CsPbI$_3$: (a) side views, (b) phonon band dispersions, and (c) electronic band dispersion of Cs$_2$PbI$_4$.[150] Reprinted with permission from Ozen *et al.* Comput. Condens. Mater. 23:e00453 2020. Copyright 2020 Elsevier B. V.

Electronic band dispersion shows that similar to thicker forms, CBM and VBM of Cs$_2$PbI$_4$.possess at Γ point. The thinnest form of orthorhombic CsPbI$_3$ is a direct bandgap semiconductor with a 2.9 eV bandgap. Bader charge analysis reveals that each Cs and Pb atom donates 0.79 and 0.75 *e* charge to surface and inner I atoms that receive 0.64 and 0.52 *e* charge, respectively.

4.2.4. Encapsulation and Thermal Stability

To increase the stability of perovskites against light and moisture, one of the commonly used methods is the encapsulation. On the other hand, maintaining optical properties and enhancing stability without decreasing the efficiency of the material may be the key to use perovskites on optoelectronic devices.[151, 152] In this regard, recently synthesized SnS_2[153] may be proper material for encapsulation of thinnest orthorhombic structure due to its quite matching lattice parameters.

Initial   Final
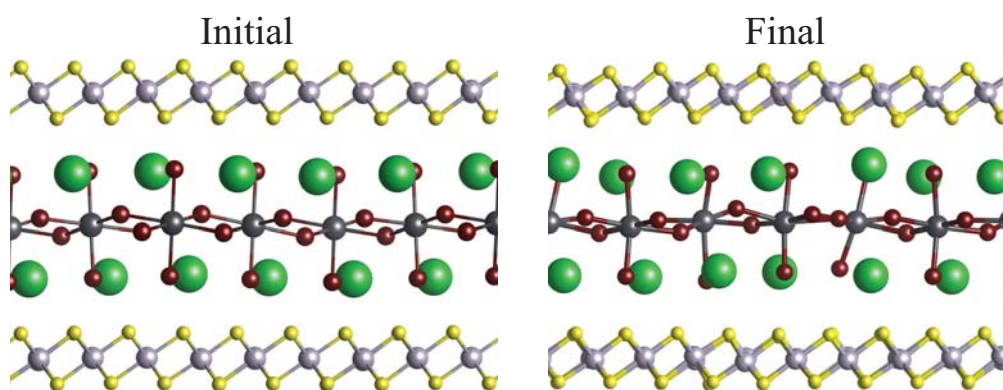
Figure 4.11. Molecular dynamics simulation of Cs_2PbI_4 structure: (a) Initial, (b) 300 K for 5 ps.[150] Reprinted with permission from Ozen *et al.* Comput. Condens. Mater. 23:e00453 2020. Copyright 2020 Elsevier B. V.

Therefore, we constructed a heterostructure and investigated its thermal stability by molecular dynamics (MD) simulations. The heterostructure was constructed by placing $2\times2\times1$ supercell of Cs_2PbI_4 between two $2\times3\times1$ rectangular 1T-SnS_2 supercells. In order to examine the thermal stability of the SnS_2-encapsulated monolayer we set the temperature of the system is kept at 300 K for 5 ps with a time step of 1 fs.

Fig. 4.11 presents the initial and final geometric structures from the side view. Thanks to the SnS_2 layers, highly mobile Cs atoms localize at small areas and structure remains stable up to 300 K. Obviously, small distortions on $[PbI_6]^{-4}$ octahedrals can be seen, but SnS_2 layers remain robust even the temperature is increased and retain the structure from breaking down. In addition, the SnS_2 layer not only prevents degradation but also protects the surfaces of the material against oxidation, moisture, and impurities.

CHAPTER 5

CONCLUSION

An increase in the energy requirement of humanity has steered scientists to discovering new two-dimensional semiconductor materials besides renewable energy sources. In this search, Cs-LHPs have come to the fore as a promising class of semiconductor materials. Since the working principle of solar cells and photodetectors are based on detection of the light, their low bandgap energies and wide absorption ranges are desired properties for light detecting applications. On the other hand, tunability of their emission color enables the production of LEDs in a wide color range. In order to use Cs-LHPs in optoelectronic device applications, increasing their stability and tuning their optical properties are crucial. Therefore, within this thesis study, we tune the optical properties of Cs-LHPs and increase their stability by using doping and thickness modification strategies.

First, Cr^{3+} doped $CsPbBr_3$ perovskites have been obtained by using a room-temperature synthesis method. SEM images, XRD measurements and simulations confirm the Cr^{3+} induced phase transition from Cs_4PbBr_6 to the $CsPbBr_xCl_{3-x}$.[108] On the other hand, incorporation of the Cr^{3+} ions into the lattice causes multiple emission peaks to emerge. The origin of additional PL peaks are identified as midgap states and strained host lattice. The DFT based electronic band dispersion calculations verify the presence of Cr^{3+} induced midgap states. Moreover, due to the strong interaction of the Cl^- including domains with the moisture, the PL intensity corresponding to $CsPbBr_xCl_{3-x}$ crystals is reduced dramatically in time and Cr doped samples start to exhibit clear white light emission with a high CRI. These findings reveal that the heterovalent doping by Cr^{3+} ion is a promising way to generate single-phase white light emission.

Second, to increase the stability of metastable α-$CsPbI_3$ structure and retard its phase transition to the room temperature stable non-perovskite yellow phase (δ-$CsPbI_3$), doping strategy is introduced by using various amounts of Gd^{3+} ions.[111] The peak shift to the higher 2θ values and the peak splitting in the XRD reflections confirmed the substitution of Gd^{3+} ions into the host lattices. Performed XRD simulations were also consistent with the experimental results. Total energy calculations reveal that the formation of the

Gd^{3+}-doped structure is more favorable than that of the bare structure. Also, a Gd^{3+} originated shrinkage of the host lattices, is verified by geometric optimization calculations. Time dependent XRD measurements and the images of the neat and Gd10 sample show that the Gd10 sample remains its α-CsPbI$_3$ phase up to 5 days. Also, dopant induced modifications are investigated by photoluminescence, PLQY, lifetime measurements, and Urbach energy analyses. It is shown that the Gd^{3+} doping decreases the defect density, provides enhancement on optical properties, and increases the stability of α-CsPbI$_3$ nanocubes.

Third, we used the single-step electrospraying method to synthesize CsPbBr$_3$ perovskites.[147] The synthesis and coating process is performed by spraying the precursor solution through ITO coated glass substrates under the electric field. STEM images and the absorption spectrum confirms the formation of CsPbBr$_3$ nanoplatelets. Since the OLAM acts as intercalating agent between nanoplatelets, we tuned the thickness of CsPbBr$_3$ perovskite nanoplatelets by altering the OLAM ratio of the precursor solution. as a result of the quantum size effect we obtained blue, cyan, and green emitting perovkite nanoplatelets. On the other hand, we performed a millimeter-sized coating process that unveils the potential of this technique to be used in patterned optoelectronic device fabrications.

Lastly, based on first-principles calculations, we investigated thickness dependency of characteristic properties of the orthorhombic CsPbI$_3$ structure.[150] Phonon calculations reveal that bilayer and monolayer forms with Cs-I terminated surfaces may form dynamically stable ultra-thin structures. Electronic band dispersion analyses revealed that regardless of the thickness, VBM and CBM of all structures possess at the Γ symmetry point. However, the bandgap energy increases with the decrease in the thickness of the perovskite. Finally, to obtain heat protection, we encapsulated the CsPbI$_3$ monolayer between SnS$_2$ layers. Molecular dynamics simulations reveal that the well-protection of the encapsulated monolayer structure is obtained at 500 °K. It is clearly shown that orthorhombic CsPbI$_3$ is a suitable candidate for future light detection applications due to its thickness-dependent properties and high thermal stability.

In conclusion, experimental and theoretical results of the functionalization of cesium lead halide perovskites by doping and dimensional modifications are presented in this thesis study. Additional emission peaks and single-phase white light emission from

CsPbBr$_x$Cl$_{3-x}$ is achieved by Cr^{3+} doping. The stability of α-CsPbI$_3$ increases by intercalation Gd^{3+} ions to the host lattice. Also, Gd^{3+} doping increases the PLQY and lifetime of the CsPbI$_3$ nanocubes. Furthermore, CsPbBr$_3$ nanoplatelets are synthesized by electrospraying and tunability of the emission color of nanoplatelets provided by thickness modification. Lastly, thickness-dependent optical and structural properties of bulk CsPbI$_3$ structure are investigated by using density functional theory-based calculations. Possible ultra-thin direct-bandgap forms of orthorhombic CsPbI$_3$ structure are presented. I believe that the results presented in this thesis will contribute to the functionalization of perovskites in order to make them more suitable for optoelectronic devices.

REFERENCES

[1] Gustav Rose. Beschreibung einiger neuen mineralien des urals. *Annalen der Physik*, 124(12):551–573, (1839).

[2] Victor Moritz Goldschmidt. Die gesetze der krystallochemie. *Naturwissenschaften*, 14(21):477–485, (1926).

[3] Dieter Weber. Ch3nh3pbx3, ein pb (ii)-system mit kubischer perowskitstruktur/ch3nh3pbx3, a pb (ii)-system with cubic perovskite structure. *Zeitschrift für Naturforschung B*, 33(12):1443–1445, (1978).

[4] Cherie R. Kagan, David B. Mitzi, and Christos D. Dimitrakopoulos. Organic-inorganic hybrid materials as semiconducting channels in thin-film field-effect transistors. *Science*, 286(5441):945–947, (1999).

[5] Akihiro Kojima, Kenjiro Teshima, Yasuo Shirai, and Tsutomu Miyasaka. Organometal halide perovskites as visible-light sensitizers for photovoltaic cells. *Journal of the American Chemical Society*, 131(17):6050–6051, (2009).

[6] Woon Seok Yang, Byung-Wook Park, Eui Hyuk Jung, Nam Joong Jeon, Young Chan Kim, Dong Uk Lee, Seong Sik Shin, Jangwon Seo, Eun Kyu Kim, Jun Hong Noh, et al. Iodide management in formamidinium-lead-halide–based perovskite layers for efficient solar cells. *Science*, 356(6345):1376–1379, (2017).

[7] Takayuki Chiba, Yukihiro Hayashi, Hinako Ebe, Keigo Hoshi, Jun Sato, Shugo Sato, Yong-Jin Pu, Satoru Ohisa, and Junji Kido. Anion-exchange red perovskite quantum dots with ammonium iodine salts for highly efficient light-emitting devices. *Nature Photonics*, 12(11):681, (2018).

[8] Yu Cao, Nana Wang, He Tian, Jingshu Guo, Yingqiang Wei, Hong Chen, Yanfeng Miao, Wei Zou, Kang Pan, Yarong He, et al. Perovskite light-emitting diodes based on spontaneously formed submicrometre-scale structures. *Nature*,

562(7726):249, (2018).

[9] Makhsud I. Saidaminov, Valerio Adinolfi, Riccardo Comin, Ahmed L. Abdelhady, Wei Peng, Ibrahim Dursun, Mingjian Yuan, Sjoerd Hoogland, Edward H. Sargent, and Osman M. Bakr. Planar-integrated single-crystalline perovskite photodetectors. *Nature communications*, 6(1):1–7, (2015).

[10] Zhipeng Lian, Qingfeng Yan, Qianrui Lv, Ying Wang, Lili Liu, Lijing Zhang, Shilie Pan, Qiang Li, Liduo Wang, and Jia-Lin Sun. High-performance planar-type photodetector on (100) facet of mapbi 3 single crystal. *Scientific reports*, 5:16563, (2015).

[11] Shreetu Shrestha, René Fischer, Gebhard J. Matt, Patrick Feldner, Thilo Michel, Andres Osvet, Ievgen Levchuk, Benoit Merle, Saeedeh Golkar, Haiwei Chen, et al. High-performance direct conversion x-ray detectors based on sintered hybrid lead triiodide perovskite wafers. *Nature Photonics*, 11(7):436–440, (2017).

[12] Haotong Wei, Dylan DeSantis, Wei Wei, Yehao Deng, Dengyang Guo, Tom J. Savenije, Lei Cao, and Jinsong Huang. Dopant compensation in alloyed ch 3 nh 3 pbbr 3- x cl x perovskite single crystals for gamma-ray spectroscopy. *Nature materials*, 16(8):826–833, (2017).

[13] Horace Lemuel Wells. Art. xvi.–on the coesium-and the potassium-lead halides. *American Journal of Science (1880-1910)*, 45(266):121, (1893).

[14] Christian K. MØLLER. A phase transition in cæsium plumbochloride. *Nature*, 180(4593):981–982, (1957).

[15] Christian K. MØLLER. Crystal structure and photoconductivity of caesium plumbohalides. *Nature*, 182(4647):1436–1436, (1958).

[16] Anthony M. Glazer. The classification of tilted octahedra in perovskites. *Acta Crystallographica Section B: Structural Crystallography and Crystal Chemistry*, 28(11):3384–3392, (1972).

[17] Michael W. Lufaso and Patrick M. Woodward. Jahn–teller distortions, cation ordering and octahedral tilting in perovskites. *Acta Crystallographica Section B: Structural Science*, 60(1):10–20, (2004).

[18] Loredana Protesescu, Sergii Yakunin, Maryna I. Bodnarchuk, Franziska Krieg, Riccarda Caputo, Christopher H. Hendon, Ruo Xi Yang, Aron Walsh, and Maksym V. Kovalenko. Nanocrystals of cesium lead halide perovskites (cspbx3, x= cl, br, and i): novel optoelectronic materials showing bright emission with wide color gamut. *Nano letters*, 15(6):3692–3696, (2015).

[19] Maksym V. Kovalenko, Loredana Protesescu, and Maryna I. Bodnarchuk. Properties and potential optoelectronic applications of lead halide perovskite nanocrystals. *Science*, 358(6364):745–750, (2017).

[20] Giles E. Eperon, Giuseppe M. Paterno, Rebecca J. Sutton, Andrea Zampetti, Amir Abbas Haghighirad, Franco Cacialli, and Henry J. Snaith. Inorganic caesium lead iodide perovskite solar cells. *Journal of Materials Chemistry A*, 3(39):19688–19695, (2015).

[21] Makhsud I. Saidaminov, Md Azimul Haque, Maxime Savoie, Ahmed L. Abdelhady, Namchul Cho, Ibrahim Dursun, Ulrich Buttner, Erkki Alarousu, Tom Wu, and Osman M. Bakr. Perovskite photodetectors operating in both narrowband and broadband regimes. *Advanced Materials*, 28(37):8144–8149, (2016).

[22] Jizhong Song, Jianhai Li, Xiaoming Li, Leimeng Xu, Yuhui Dong, and Haibo Zeng. Quantum dot light-emitting diodes based on inorganic perovskite cesium lead halides (cspbx3). *Advanced materials*, 27(44):7162–7167, (2015).

[23] Xiaoming Li, Fei Cao, Dejian Yu, Jun Chen, Zhiguo Sun, Yalong Shen, Ying Zhu, Lin Wang, Yi Wei, Ye Wu, et al. All inorganic halide perovskites nanosystem: synthesis, structural features, optical properties and optoelectronic applications. *Small*, 13(9):1603996, (2017).

[24] Bin Luo, Gang Liu, and Lianzhou Wang. Recent advances in 2d materials for photo-

catalysis. *Nanoscale*, 8(13):6904–6920, (2016).

[25] Gang Liu, Yanning Zhao, Chenghua Sun, Feng Li, Gao Qing Lu, and Hui-Ming Cheng. Synergistic effects of b/n doping on the visible-light photocatalytic activity of mesoporous tio2. *Angewandte Chemie International Edition*, 47(24):4516–4520, (2008).

[26] Aniruddh Mukherji, Roland Marschall, Akshat Tanksale, Chenghua Sun, Sean C. Smith, Gao Qing Lu, and Lianzhou Wang. N-doped cstawo6 as a new photocatalyst for hydrogen production from water splitting under solar irradiation. *Advanced Functional Materials*, 21(1):126–132, (2011).

[27] Xu Zong, Zheng Xing, Hua Yu, Zhigang Chen, Fengqiu Tang, Jin Zou, Gao Qing Lu, and Lianzhou Wang. Photocatalytic water oxidation on f, n co-doped tio 2 with dominant exposed {001} facets under visible light. *Chemical Communications*, 47(42):11742–11744, (2011).

[28] Yasumichi Matsumoto, Michio Koinuma, Yoshifumi Iwanaga, Tetsuya Sato, and Shintaro Ida. N doping of oxide nanosheets. *Journal of the American Chemical Society*, 131(19):6644–6645, (2009).

[29] Yu Fu, Chun Chang, Peng Chen, Xiaolong Chu, and Lingyan Zhu. Enhanced photocatalytic performance of boron doped bi2wo6 nanosheets under simulated solar light irradiation. *Journal of hazardous materials*, 254:185–192, (2013).

[30] Quanjun Xiang, Jiaguo Yu, and Mietek Jaroniec. Nitrogen and sulfur co-doped tio 2 nanosheets with exposed {001} facets: synthesis, characterization and visible-light photocatalytic activity. *Physical Chemistry Chemical Physics*, 13(11):4853–4861, (2011).

[31] Yajun Zhou, Lingxia Zhang, Jianjun Liu, Xiangqian Fan, Beizhou Wang, Min Wang, Wenchao Ren, Jin Wang, Mengli Li, and Jianlin Shi. Brand new p-doped gc 3 n 4: enhanced photocatalytic activity for h 2 evolution and rhodamine b degradation under visible light. *Journal of Materials Chemistry A*, 3(7):3862–3867, (2015).

[32] Jingrun Ran, Tian Yi Ma, Guoping Gao, Xi-Wen Du, and Shi Zhang Qiao. Porous p-doped graphitic carbon nitride nanosheets for synergistically enhanced visible-light photocatalytic h 2 production. *Energy & Environmental Science*, 8(12):3708–3717, (2015).

[33] Abhishek Swarnkar, Wasim J. Mir, and Angshuman Nag. Can b-site doping or alloying improve thermal-and phase-stability of all-inorganic cspbx3 (x= cl, br, i) perovskites? *ACS Energy Letters*, 3(2):286–289, (2018).

[34] Jun Yin, Ghada H. Ahmed, Osman M. Bakr, Jean-Luc Brédas, and Omar F. Mohammed. Unlocking the effect of trivalent metal doping in all-inorganic cspbbr3 perovskite. *ACS Energy Letters*, 4(3):789–795, (2019).

[35] Jialong Duan, Yuanyuan Zhao, Xiya Yang, Yudi Wang, Benlin He, and Qunwei Tang. Lanthanide ions doped cspbbr3 halides for htm-free 10.14%-efficiency inorganic perovskite solar cell with an ultrahigh open-circuit voltage of 1.594 v. *Advanced Energy Materials*, 8(31):1802346, (2018).

[36] Qingsong Hu, Zha Li, Zhifang Tan, Huaibing Song, Cong Ge, Guangda Niu, Jiantao Han, and Jiang Tang. Rare earth ion-doped cspbbr3 nanocrystals. *Advanced Optical Materials*, 6(2):1700864, (2018).

[37] Narayan Pradhan, Samrat Das Adhikari, Angshuman Nag, and Dipankar D. Sarma. Luminescence, plasmonic, and magnetic properties of doped semiconductor nanocrystals. *Angewandte Chemie International Edition*, 56(25):7038–7054, (2017).

[38] Quinten A. Akkerman, Daniele Meggiolaro, Zhiya Dang, Filippo De Angelis, and Liberato Manna. Fluorescent alloy cspb x mn1-xi3 perovskite nanocrystals with high structural and optical stability. *ACS energy letters*, 2(9):2183–2186, (2017).

[39] Dongliang Bai, Jingru Zhang, Zhiwen Jin, Hui Bian, Kang Wang, Haoran Wang, Lei Liang, Qian Wang, and Shengzhong Frank Liu. Interstitial mn2+-driven high-aspect-ratio grain growth for low-trap-density microcrystalline films for record

efficiency cspbi2br solar cells. *ACS Energy Letters*, 3(4):970–978, (2018).

[40] Tugrul Guner, Baris Akbali, Mehmet Ozcan, Gokhan Topcu, Mustafa M. Demir, and Hasan Sahin. Monitoring the doping and diffusion characteristics of mn dopants in cesium lead halide perovskites. *The Journal of Physical Chemistry C*, 122(21):11543–11549, (2018).

[41] Feng Liu, Chao Ding, Yaohong Zhang, Teresa S. Ripolles, Taichi Kamisaka, Taro Toyoda, Shuzi Hayase, Takashi Minemoto, Kenji Yoshino, Songyuan Dai, et al. Colloidal synthesis of air-stable alloyed cssn1–x pb x i3 perovskite nanocrystals for use in solar cells. *Journal of the American Chemical Society*, 139(46):16708–16719, (2017).

[42] Xinyu Shen, Yu Zhang, Stephen V. Kershaw, Tianshu Li, Congcong Wang, Xiaoyu Zhang, Wenyan Wang, Daguang Li, Yinghui Wang, Min Lu, et al. Zn-alloyed cspbi3 nanocrystals for highly efficient perovskite light-emitting devices. *Nano letters*, 19(3):1552–1559, (2019).

[43] Feng Liu, Chao Ding, Yaohong Zhang, Taichi Kamisaka, Qian Zhao, Joseph M. Luther, Taro Toyoda, Shuzi Hayase, Takashi Minemoto, Kenji Yoshino, et al. Gei2 additive for high optoelectronic quality cspbi3 quantum dots and their application in photovoltaic devices. *Chemistry of Materials*, 31(3):798–807, (2019).

[44] Cho Fai Jonathan Lau, Meng Zhang, Xiaofan Deng, Jianghui Zheng, Jueming Bing, Qingshan Ma, Jincheol Kim, Long Hu, Martin A. Green, Shujuan Huang, et al. Strontium-doped low-temperature-processed cspbi2br perovskite solar cells. *ACS Energy Letters*, 2(10):2319–2325, (2017).

[45] Gencai Pan, Xue Bai, Dongwen Yang, Xu Chen, Pengtao Jing, Songnan Qu, Lijun Zhang, Donglei Zhou, Jinyang Zhu, Wen Xu, et al. Doping lanthanide into perovskite nanocrystals: highly improved and expanded optical properties. *Nano letters*, 17(12):8005–8011, (2017).

[46] Ming Liu, Guohua Zhong, Yongming Yin, Jingsheng Miao, Ke Li, Chengqun Wang,

Xiuru Xu, Clifton Shen, and Hong Meng. Aluminum-doped cesium lead bromide perovskite nanocrystals with stable blue photoluminescence used for display backlight. *Advanced Science*, 4(11):1700335, (2017).

[47] Ji-Song Yao, Jing Ge, Bo-Ning Han, Kun-Hua Wang, Hong-Bin Yao, Hao-Lei Yu, Jian-Hai Li, Bai-Sheng Zhu, Ji-Zhong Song, Chen Chen, et al. Ce3+-doping to modulate photoluminescence kinetics for efficient cspbbr3 nanocrystals based light-emitting diodes. *Journal of the American Chemical Society*, 140(10):3626–3634, (2018).

[48] Wanchun Xiang, Zaiwei Wang, Dominik J. Kubicki, Wolfgang Tress, Jingshan Luo, Daniel Prochowicz, Seckin Akin, Lyndon Emsley, Jiangtao Zhou, Giovanni Dietler, et al. Europium-doped cspbi2br for stable and highly efficient inorganic perovskite solar cells. *Joule*, 3(1):205–214, (2019).

[49] Yanqiang Hu, Fan Bai, Xinbang Liu, Qingmin Ji, Xiaoliang Miao, Ting Qiu, and Shufang Zhang. Bismuth incorporation stabilized α-cspbi3 for fully inorganic perovskite solar cells. *ACS Energy Letters*, 2(10):2219–2227, (2017).

[50] Olga A. Lozhkina, Anna A. Murashkina, Vladimir V. Shilovskikh, Yury V. Kapitonov, Vladimir K. Ryabchuk, Alexei V. Emeline, and Tsutomu Miyasaka. Invalidity of band-gap engineering concept for bi3+ heterovalent doping in cspbbr3 halide perovskite. *The journal of physical chemistry letters*, 9(18):5408–5411, (2018).

[51] Ajay Kumar Jena, Ashish Kulkarni, Yoshitaka Sanehira, Masashi Ikegami, and Tsutomu Miyasaka. Stabilization of α-cspbi3 in ambient room temperature conditions by incorporating eu into cspbi3. *Chemistry of Materials*, 30(19):6668–6674, (2018).

[52] Xiangtong Zhang, Yu Zhang, Xiaoyu Zhang, Wenxu Yin, Yu Wang, Hua Wang, Min Lu, Zhiyang Li, Zhiyong Gu, and W. Yu William. Yb 3+ and yb 3+/er 3+ doping for near-infrared emission and improved stability of cspbcl 3 nanocrystals. *Journal of Materials Chemistry C*, 6(37):10101–10105, (2018).

[53] Xiangtong Zhang, Hua Wang, Yue Hu, Yixian Pei, Shixun Wang, Zhifeng Shi, Vicki L. Colvin, Shengnian Wang, Yu Zhang, and William W. Yu. Strong blue emission from sb3+-doped super small cspbbr3 nanocrystals. *The journal of physical chemistry letters*, 10(8):1750–1756, (2019).

[54] Georgian Nedelcu, Loredana Protesescu, Sergii Yakunin, Maryna I. Bodnarchuk, Matthias J. Grotevent, and Maksym V. Kovalenko. Fast anion-exchange in highly luminescent nanocrystals of cesium lead halide perovskites (cspbx3, x= cl, br, i). *Nano letters*, 15(8):5635–5640, (2015).

[55] Quinten A. Akkerman, Valerio D'Innocenzo, Sara Accornero, Alice Scarpellini, Annamaria Petrozza, Mirko Prato, and Liberato Manna. Tuning the optical properties of cesium lead halide perovskite nanocrystals by anion exchange reactions. *Journal of the American Chemical Society*, 137(32):10276–10281, (2015).

[56] Sandeep Pathak, Nobuya Sakai, Florencia Wisnivesky Rocca Rivarola, Samuel D. Stranks, Jiewei Liu, Giles E. Eperon, Caterina Ducati, Konrad Wojciechowski, James T. Griffiths, Amir Abbas Haghighirad, et al. Perovskite crystals for tunable white light emission. *Chemistry of Materials*, 27(23):8066–8075, (2015).

[57] Dandan Zhang, Yiming Yang, Yehonadav Bekenstein, Yi Yu, Natalie A. Gibson, Andrew B. Wong, Samuel W. Eaton, Nikolay Kornienko, Qiao Kong, Minliang Lai, et al. Synthesis of composition tunable and highly luminescent cesium lead halide nanowires through anion-exchange reactions. *Journal of the American Chemical Society*, 138(23):7236–7239, (2016).

[58] Norman Pellet, Peng Gao, Giuliano Gregori, Tae-Youl Yang, Mohammad K. Nazeeruddin, Joachim Maier, and Michael Grätzel. Mixed-organic-cation perovskite photovoltaics for enhanced solar-light harvesting. *Angewandte Chemie International Edition*, 53(12):3151–3157, (2014).

[59] Dongqin Bi, Wolfgang Tress, M. Ibrahim Dar, Peng Gao, Jingshan Luo, Clémentine Renevier, Kurt Schenk, Antonio Abate, Fabrizio Giordano, Juan-Pablo Correa Baena, et al. Efficient luminescent solar cells based on tailored mixed-cation per-

ovskites. *Science advances*, 2(1):e1501170, (2016).

[60] Amit K. Guria, Sumit K. Dutta, Samrat Das Adhikari, and Narayan Pradhan. Doping mn2+ in lead halide perovskite nanocrystals: successes and challenges. *ACS Energy Letters*, 2(5):1014–1021, (2017).

[61] Yang Zhou, Jie Chen, Osman M. Bakr, and Hong-Tao Sun. Metal-doped lead halide perovskites: synthesis, properties, and optoelectronic applications. *Chemistry of Materials*, 30(19):6589–6613, (2018).

[62] Abhishek Swarnkar, Vikash Kumar Ravi, and Angshuman Nag. Beyond colloidal cesium lead halide perovskite nanocrystals: analogous metal halides and doping. *ACS Energy Letters*, 2(5):1089–1098, (2017).

[63] Wenyong Liu, Qianglu Lin, Hongbo Li, Kaifeng Wu, István Robel, Jeffrey M. Pietryga, and Victor I. Klimov. Mn2+-doped lead halide perovskite nanocrystals with dual-color emission controlled by halide content. *Journal of the American Chemical Society*, 138(45):14954–14961, (2016).

[64] He Shao, Xue Bai, Haining Cui, Gencai Pan, Pengtao Jing, Songnan Qu, Jinyang Zhu, Yue Zhai, Biao Dong, and Hongwei Song. White light emission in bi 3+/mn 2+ ion co-doped cspbcl 3 perovskite nanocrystals. *Nanoscale*, 10(3):1023–1029, (2018).

[65] Shenghan Zou, Yongsheng Liu, Jianhai Li, Caiping Liu, Rui Feng, Feilong Jiang, Yongxiang Li, Jizhong Song, Haibo Zeng, Maochun Hong, et al. Stabilizing cesium lead halide perovskite lattice through mn (ii) substitution for air-stable light-emitting diodes. *Journal of the American Chemical Society*, 139(33):11443–11450, (2017).

[66] Subham Dastidar, David A. Egger, Liang Z. Tan, Samuel B. Cromer, Andrew D. Dillon, Shi Liu, Leeor Kronik, Andrew M. Rappe, and Aaron T. Fafarman. High chloride doping levels stabilize the perovskite phase of cesium lead iodide. *Nano letters*, 16(6):3563–3570, (2016).

[67] Constantinos C. Stoumpos, Christos D. Malliakas, John A. Peters, Zhifu Liu, Maria Sebastian, Jino Im, Thomas C. Chasapis, Arief C. Wibowo, Duck Young Chung, Arthur J. Freeman, et al. Crystal growth of the perovskite semiconductor cspbbr3: a new material for high-energy radiation detection. *Crystal growth & design*, 13(7):2722–2727, (2013).

[68] Jizhong Song, Qingzhi Cui, Jianhai Li, Jiayue Xu, Yue Wang, Leimeng Xu, Jie Xue, Yuhui Dong, Tian Tian, Handong Sun, et al. Ultralarge all-inorganic perovskite bulk single crystal for high-performance visible–infrared dual-modal photodetectors. *Advanced Optical Materials*, 5(12):1700157, (2017).

[69] Dmitry N. Dirin, Ihor Cherniukh, Sergii Yakunin, Yevhen Shynkarenko, and Maksym V. Kovalenko. Solution-grown cspbbr3 perovskite single crystals for photon detection. *Chemistry of Materials*, 28(23):8470–8474, (2016).

[70] Makhsud I. Saidaminov, Md Azimul Haque, Jawaher Almutlaq, Smritakshi Sarmah, Xiao-He Miao, Raihana Begum, Ayan A. Zhumekenov, Ibrahim Dursun, Namchul Cho, Banavoth Murali, et al. Inorganic lead halide perovskite single crystals: phase-selective low-temperature growth, carrier transport properties, and self-powered photodetection. *Advanced Optical Materials*, 5(2):1600704, (2017).

[71] Yevgeny Rakita, Nir Kedem, Satyajit Gupta, Aditya Sadhanala, Vyacheslav Kalchenko, Marcus L. Böhm, Michael Kulbak, Richard H. Friend, David Cahen, and Gary Hodes. Low-temperature solution-grown cspbbr3 single crystals and their characterization. *Crystal Growth & Design*, 16(10):5717–5725, (2016).

[72] Javad Shamsi, Zhiya Dang, Paolo Bianchini, Claudio Canale, Francesco Di Stasio, Rosaria Brescia, Mirko Prato, and Liberato Manna. Colloidal synthesis of quantum confined single crystal cspbbr3 nanosheets with lateral size control up to the micrometer range. *Journal of the American Chemical Society*, 138(23):7240–7243, (2016).

[73] Yehonadav Bekenstein, Brent A. Koscher, Samuel W. Eaton, Peidong Yang, and A. Paul Alivisatos. Highly luminescent colloidal nanoplates of perovskite cesium

lead halide and their oriented assemblies. *Journal of the American Chemical Society*, 137(51):16008–16011, (2015).

[74] Dandan Zhang, Samuel W. Eaton, Yi Yu, Letian Dou, and Peidong Yang. Solution-phase synthesis of cesium lead halide perovskite nanowires. *Journal of the American Chemical Society*, 137(29):9230–9233, (2015).

[75] Shibin Sun, Dan Yuan, Yuan Xu, Aifei Wang, and Zhengtao Deng. Ligand-mediated synthesis of shape-controlled cesium lead halide perovskite nanocrystals via re-precipitation process at room temperature. *ACS nano*, 10(3):3648–3657, (2016).

[76] Jasmina A. Sichert, Yu Tong, Niklas Mutz, Mathias Vollmer, Stefan Fischer, Karolina Z. Milowska, Ramon García Cortadella, Bert Nickel, Carlos Cardenas-Daw, Jacek K. Stolarczyk, et al. Quantum size effect in organometal halide perovskite nanoplatelets. *Nano letters*, 15(10):6521–6527, (2015).

[77] Dandan Zhang, Yi Yu, Yehonadav Bekenstein, Andrew B. Wong, A. Paul Alivisatos, and Peidong Yang. Ultrathin colloidal cesium lead halide perovskite nanowires. *Journal of the American Chemical Society*, 138(40):13155–13158, (2016).

[78] Michael C. Brennan, Jessica Zinna, and Masaru Kuno. Existence of a size-dependent stokes shift in cspbbr3 perovskite nanocrystals. *ACS Energy Letters*, 2(7):1487–1488, (2017).

[79] Eitan Oksenberg, Ella Sanders, Ronit Popovitz-Biro, Lothar Houben, and Ernesto Joselevich. Surface-guided cspbbr3 perovskite nanowires on flat and faceted sapphire with size-dependent photoluminescence and fast photoconductive response. *Nano letters*, 18(1):424–433, (2018).

[80] Wan-Jian Yin, Ji-Hui Yang, Joongoo Kang, Yanfa Yan, and Su-Huai Wei. Halide perovskite materials for solar cells: a theoretical review. *Journal of Materials Chemistry A*, 3(17):8926–8942, (2015).

[81] Jun Haruyama, Keitaro Sodeyama, Liyuan Han, and Yoshitaka Tateyama. First-

principles study of ion diffusion in perovskite solar cell sensitizers. *Journal of the American Chemical Society*, 137(32):10048–10051, (2015).

[82] Wei Geng, Le Zhang, Yan-Ning Zhang, Woon-Ming Lau, and Li-Min Liu. First-principles study of lead iodide perovskite tetragonal and orthorhombic phases for photovoltaics. *The Journal of Physical Chemistry C*, 118(34):19565–19571, (2014).

[83] Hiroki Kawai, Giacomo Giorgi, Andrea Marini, and Koichi Yamashita. The mechanism of slow hot-hole cooling in lead-iodide perovskite: first-principles calculation on carrier lifetime from electron–phonon interaction. *Nano letters*, 15(5):3103–3108, (2015).

[84] Fadıl İyikanat, Emre Sari, and Hasan Sahin. Thinning cspb 2 br 5 perovskite down to monolayers: Cs-dependent stability. *Physical Review B*, 96(15):155442, (2017).

[85] Alejandro Molina-Sánchez. Excitonic states in semiconducting two-dimensional perovskites. *ACS Applied Energy Materials*, 1(11):6361–6367, (2018).

[86] Xiaoming Li, Ye Wu, Shengli Zhang, Bo Cai, Yu Gu, Jizhong Song, and Haibo Zeng. Cspbx3 quantum dots for lighting and displays: room-temperature synthesis, photoluminescence superiorities, underlying origins and white light-emitting diodes. *Advanced Functional Materials*, 26(15):2435–2445, (2016).

[87] Jingrun Zhu, Xiaoling Yang, Yihua Zhu, Yuanwei Wang, Jin Cai, Jianhua Shen, Luyi Sun, and Chunzhong Li. Room-temperature synthesis of mn-doped cesium lead halide quantum dots with high mn substitution ratio. *The journal of physical chemistry letters*, 8(17):4167–4171, (2017).

[88] Georg Kresse and Jürgen Hafner. Ab initio molecular dynamics for liquid metals. *Physical Review B*, 47(1):558, (1993).

[89] Georg Kresse and Jürgen Furthmüller. Efficient iterative schemes for ab initio total-energy calculations using a plane-wave basis set. *Physical review B*,

54(16):11169, (1996).

[90] Walter Kohn and Lu Jeu Sham. Self-consistent equations including exchange and correlation effects. *Physical review*, 140(4A):A1133, (1965).

[91] Peter E. Blöchl. Projector augmented-wave method. *Physical review B*, 50(24):17953, (1994).

[92] Georg Kresse and Daniel Joubert. From ultrasoft pseudopotentials to the projector augmented-wave method. *Physical review b*, 59(3):1758, (1999).

[93] John P. Perdew, Kieron Burke, and Matthias Ernzerhof. Generalized gradient approximation made simple. *Physical review letters*, 77(18):3865, (1996).

[94] John P. Perdew and Alex Zunger. Self-interaction correction to density-functional approximations for many-electron systems. *Physical Review B*, 23(10):5048, (1981).

[95] Stefan Grimme. Semiempirical gga-type density functional constructed with a long-range dispersion correction. *Journal of computational chemistry*, 27(15):1787–1799, (2006).

[96] Graeme Henkelman, Andri Arnaldsson, and Hannes Jónsson. A fast and robust algorithm for bader decomposition of charge density. *Computational Materials Science*, 36(3):354–360, (2006).

[97] Atsushi Togo, Fumiyasu Oba, and Isao Tanaka. First-principles calculations of the ferroelastic transition between rutile-type and cacl 2-type sio 2 at high pressures. *Physical Review B*, 78(13):134106, (2008).

[98] Nikolay S. Makarov, Shaojun Guo, Oleksandr Isaienko, Wenyong Liu, István Robel, and Victor I. Klimov. Spectral and dynamical properties of single excitons, biexcitons, and trions in cesium–lead-halide perovskite quantum dots. *Nano letters*, 16(4):2349–2362, (2016).

[99] Cunlong Li, Zhigang Zang, Weiwei Chen, Zhiping Hu, Xiaosheng Tang, Wei Hu, Kuan Sun, Xianming Liu, and Weimin Chen. Highly pure green light emission of perovskite cspbbr 3 quantum dots and their application for green light-emitting diodes. *Optics express*, 24(13):15071–15078, (2016).

[100] Dongdong Yan, Tongchao Shi, Zhigang Zang, Tingwei Zhou, Zhengzheng Liu, Zeyu Zhang, Juan Du, Yuxin Leng, and Xiaosheng Tang. Ultrastable cspbbr3 perovskite quantum dot and their enhanced amplified spontaneous emission by surface ligand modification. *Small*, 15(23):1901173, (2019).

[101] Verena A. Hintermayr, Alexander F. Richter, Florian Ehrat, Markus Döblinger, Willem Vanderlinden, Jasmina A. Sichert, Yu Tong, Lakshminarayana Polavarapu, Jochen Feldmann, and Alexander S. Urban. Tuning the optical properties of perovskite nanoplatelets through composition and thickness by ligand-assisted exfoliation. *Advanced materials*, 28(43):9478–9485, (2016).

[102] Muhammad Imran, Vincenzo Caligiuri, Mengjiao Wang, Luca Goldoni, Mirko Prato, Roman Krahne, Luca De Trizio, and Liberato Manna. Benzoyl halides as alternative precursors for the colloidal synthesis of lead-based halide perovskite nanocrystals. *Journal of the American Chemical Society*, 140(7):2656–2664, (2018).

[103] Rebecca J. Sutton, Giles E. Eperon, Laura Miranda, Elizabeth S. Parrott, Brett A. Kamino, Jay B. Patel, Maximilian T. Hörantner, Michael B. Johnston, Amir Abbas Haghighirad, David T. Moore, et al. Bandgap-tunable cesium lead halide perovskites with high thermal stability for efficient solar cells. *Advanced Energy Materials*, 6(8):1502458, (2016).

[104] Michael Kulbak, David Cahen, and Gary Hodes. How important is the organic part of lead halide perovskite photovoltaic cells? efficient cspbbr3 cells. *The journal of physical chemistry letters*, 6(13):2452–2456, (2015).

[105] Subham Dastidar, Christopher J. Hawley, Andrew D. Dillon, Alejandro D. Gutierrez-Perez, Jonathan E. Spanier, and Aaron T. Fafarman. Quantitative phase-change

thermodynamics and metastability of perovskite-phase cesium lead iodide. *The journal of physical chemistry letters*, 8(6):1278–1282, (2017).

[106] Jun Pan, Yuequn Shang, Jun Yin, Michele De Bastiani, Wei Peng, Ibrahim Dursun, Lutfan Sinatra, Ahmed M El-Zohry, Mohamed N Hedhili, Abdul-Hamid Emwas, et al. Bidentate ligand-passivated cspbi3 perovskite nanocrystals for stable near-unity photoluminescence quantum yield and efficient red light-emitting diodes. *Journal of the American Chemical Society*, 140(2):562–565, (2017).

[107] Makhsud I. Saidaminov, Jawaher Almutlaq, Smritakshi Sarmah, Ibrahim Dursun, Ayan A. Zhumekenov, Raihana Begum, Jun Pan, Namchul Cho, Omar F. Mohammed, and Osman M. Bakr. Pure cs4pbbr6: highly luminescent zero-dimensional perovskite solids. *ACS Energy Letters*, 1(4):840–845, (2016).

[108] Sercan Ozen, Tugrul Guner, Gokhan Topcu, Mehmet Ozcan, Mustafa M. Demir, and Hasan Sahin. Experimental and first-principles investigation of cr-driven color change in cesium lead halide perovskites. *Journal of Applied Physics*, 125(22):225705, (2019).

[109] Yuhai Zhang, Makhsud I. Saidaminov, Ibrahim Dursun, Haoze Yang, Banavoth Murali, Erkki Alarousu, Emre Yengel, Buthainah A. Alshankiti, Osman M. Bakr, and Omar F. Mohammed. Zero-dimensional cs4pbbr6 perovskite nanocrystals. *The journal of physical chemistry letters*, 8(5):961–965, (2017).

[110] Zhiping Hu, Zhengzheng Liu, Yao Bian, Dongjue Liu, Xiaosheng Tang, Wei Hu, Zhigang Zang, Miao Zhou, Lidong Sun, Jianxin Tang, et al. Robust cesium lead halide perovskite microcubes for frequency upconversion lasing. *Advanced Optical Materials*, 5(22):1700419, (2017).

[111] C. Meric Guvenc, Yenal Yalcinkaya, Sercan Ozen, Hasan Sahin, and Mustafa M. Demir. Gd3+-doped α-cspbi3 nanocrystals with better phase stability and optical properties. *The Journal of Physical Chemistry C*, 123(40):24865–24872, (2019).

[112] Tugrul Guner and Mustafa M. Demir. A review on halide perovskites as color con-

version layers in white light emitting diode applications. *physica status solidi (a)*, 215(13):1800120, (2018).

[113] Zhen Li, Mengjin Yang, Ji-Sang Park, Su-Huai Wei, Joseph J. Berry, and Kai Zhu. Stabilizing perovskite structures by tuning tolerance factor: formation of formamidinium and cesium lead iodide solid-state alloys. *Chemistry of Materials*, 28(1):284–292, (2016).

[114] Chunfan Yang, Adam Faust, Yorai Amit, Itay Gdor, Uri Banin, and Sanford Ruhman. Impurity sub-band in heavily cu-doped inas nanocrystal quantum dots detected by ultrafast transient absorption. *The Journal of Physical Chemistry A*, 120(19):3088–3097, (2016).

[115] Raihana Begum, Manas R. Parida, Ahmed L. Abdelhady, Banavoth Murali, Noktan M. Alyami, Ghada H. Ahmed, Mohamed Nejib Hedhili, Osman M. Bakr, and Omar F. Mohammed. Engineering interfacial charge transfer in cspbbr3 perovskite nanocrystals by heterovalent doping. *Journal of the American Chemical Society*, 139(2):731–737, (2017).

[116] Prashant V. Kamat, Nada M. Dimitrijevic, and Arthur J. Nozik. Dynamic burstein-moss shift in semiconductor colloids. *The Journal of Physical Chemistry*, 93(8):2873–2875, (1989).

[117] Muhammad Imran, Francesco Di Stasio, Zhiya Dang, Claudio Canale, Ali Hossain Khan, Javad Shamsi, Rosaria Brescia, Mirko Prato, and Liberato Manna. Colloidal synthesis of strongly fluorescent cspbbr3 nanowires with width tunable down to the quantum confinement regime. *Chemistry of Materials*, 28(18):6450–6454, (2016).

[118] Mark C. Weidman, Michael Seitz, Samuel D. Stranks, and William A. Tisdale. Highly tunable colloidal perovskite nanoplatelets through variable cation, metal, and halide composition. *ACS nano*, 10(8):7830–7839, (2016).

[119] Franz Urbach. The long-wavelength edge of photographic sensitivity and of the elec-

tronic absorption of solids. *Physical Review*, 92(5):1324, (1953).

[120] Brandon R. Sutherland and Edward H. Sargent. Perovskite photonic sources. *Nature Photonics*, 10(5):295, (2016).

[121] Chun Sun, Yu Zhang, Cheng Ruan, Chunyang Yin, Xiaoyong Wang, Yiding Wang, and William W. Yu. Efficient and stable white leds with silica-coated inorganic perovskite quantum dots. *Advanced Materials*, 28(45):10088–10094, (2016).

[122] Rachel E. Beal, Daniel J. Slotcavage, Tomas Leijtens, Andrea R. Bowring, Rebecca A. Belisle, William H. Nguyen, George F. Burkhard, Eric T. Hoke, and Michael D. McGehee. Cesium lead halide perovskites with improved stability for tandem solar cells. *The journal of physical chemistry letters*, 7(5):746–751, (2016).

[123] Samuel W. Eaton, Minliang Lai, Natalie A. Gibson, Andrew B. Wong, Letian Dou, Jie Ma, Lin-Wang Wang, Stephen R. Leone, and Peidong Yang. Lasing in robust cesium lead halide perovskite nanowires. *Proceedings of the National Academy of Sciences*, 113(8):1993–1998, (2016).

[124] Tiebin Yang, Feng Li, and Rongkun Zheng. Recent progress on cesium lead halide perovskites for photodetection applications. *ACS Applied Electronic Materials*, 1(8):1348–1366, (2019).

[125] Xiaoming Li, Dejian Yu, Fei Cao, Yu Gu, Yi Wei, Ye Wu, Jizhong Song, and Haibo Zeng. Healing all-inorganic perovskite films via recyclable dissolution–recyrstallization for compact and smooth carrier channels of optoelectronic devices with high stability. *Advanced Functional Materials*, 26(32):5903–5912, (2016).

[126] Cunlong Li, Ceng Han, Yubo Zhang, Zhigang Zang, Ming Wang, Xiaosheng Tang, and Jihe Du. Enhanced photoresponse of self-powered perovskite photodetector based on zno nanoparticles decorated cspbbr3 films. *Solar Energy Materials and Solar Cells*, 172:341–346, (2017).

[127] Jizhong Song, Leimeng Xu, Jianhai Li, Jie Xue, Yuhui Dong, Xiaoming Li, and Haibo Zeng. Monolayer and few-layer all-inorganic perovskites as a new family of two-dimensional semiconductors for printable optoelectronic devices. *Advanced materials*, 28(24):4861–4869, (2016).

[128] Jin Hyuck Heo, Dong Hee Shin, Jin Kyoung Park, Do Hun Kim, Sang Jin Lee, and Sang Hyuk Im. High-performance next-generation perovskite nanocrystal scintillator for nondestructive x-ray imaging. *Advanced Materials*, 30(40):1801743, (2018).

[129] Wang Chen, Yunpeng Liu, Zicheng Yuan, Zhiheng Xu, Zhengrong Zhang, Kai Liu, Zhangang Jin, and Xiaobin Tang. X-ray radioluminescence effect of all-inorganic halide perovskite cspbbr 3 quantum dots. *Journal of Radioanalytical and Nuclear Chemistry*, 314(3):2327–2337, (2017).

[130] Martin Nikl and Akira Yoshikawa. Recent r&d trends in inorganic single-crystal scintillator materials for radiation detection. *Advanced Optical Materials*, 3(4):463–481, (2015).

[131] Yihui He, Liviu Matei, Hee Joon Jung, Kyle M. McCall, Michelle Chen, Constantinos C. Stoumpos, Zhifu Liu, John A Peters, Duck Young Chung, Bruce W. Wessels, et al. High spectral resolution of gamma-rays at room temperature by perovskite cspbbr 3 single crystals. *Nature communications*, 9(1):1–8, (2018).

[132] Himchan Cho, Christoph Wolf, Joo Sung Kim, Hyung Joong Yun, Jong Seong Bae, Hobeom Kim, Jung-Min Heo, Soyeong Ahn, and Tae-Woo Lee. High-efficiency solution-processed inorganic metal halide perovskite light-emitting diodes. *Advanced Materials*, 29(31):1700579, (2017).

[133] Zhanhua Wei, Ajay Perumal, Rui Su, Shendre Sushant, Jun Xing, Qing Zhang, Swee Tiam Tan, Hilmi Volkan Demir, and Qihua Xiong. Solution-processed highly bright and durable cesium lead halide perovskite light-emitting diodes. *Nanoscale*, 8(42):18021–18026, (2016).

[134] Jun Pan, Li Na Quan, Yongbiao Zhao, Wei Peng, Banavoth Murali, Smritakshi P. Sarmah, Mingjian Yuan, Lutfan Sinatra, Noktan M. Alyami, Jiakai Liu, et al. Highly efficient perovskite-quantum-dot light-emitting diodes by surface engineering. *Advanced Materials*, 28(39):8718–8725, (2016).

[135] Young-Hoon Kim, Himchan Cho, and Tae-Woo Lee. Metal halide perovskite light emitters. *Proceedings of the National Academy of Sciences*, 113(42):11694–11702, (2016).

[136] Himchan Cho, Su-Hun Jeong, Min-Ho Park, Young-Hoon Kim, Christoph Wolf, Chang-Lyoul Lee, Jin Hyuck Heo, Aditya Sadhanala, NoSoung Myoung, Seunghyup Yoo, et al. Overcoming the electroluminescence efficiency limitations of perovskite light-emitting diodes. *Science*, 350(6265):1222–1225, (2015).

[137] Qi Chen, Huanping Zhou, Tze-Bin Song, Song Luo, Ziruo Hong, Hsin-Sheng Duan, Letian Dou, Yongsheng Liu, and Yang Yang. Controllable self-induced passivation of hybrid lead iodide perovskites toward high performance solar cells. *Nano letters*, 14(7):4158–4163, (2014).

[138] Riley E. Brandt, Vladan Stevanović, David S. Ginley, and Tonio Buonassisi. Identifying defect-tolerant semiconductors with high minority-carrier lifetimes: beyond hybrid lead halide perovskites. *Mrs Communications*, 5(2):265–275, (2015).

[139] Matthew R. Leyden, Luis K. Ono, Sonia R. Raga, Yuichi Kato, Shenghao Wang, and Yabing Qi. High performance perovskite solar cells by hybrid chemical vapor deposition. *Journal of Materials Chemistry A*, 2(44):18742–18745, (2014).

[140] Mohammad Mahdi Tavakoli, Leilei Gu, Yuan Gao, Claas Reckmeier, Jin He, Andrey L. Rogach, Yan Yao, and Zhiyong Fan. Fabrication of efficient planar perovskite solar cells using a one-step chemical vapor deposition method. *Scientific reports*, 5:14083, (2015).

[141] Shuai Yuan, Zhao-Kui Wang, Ming-Peng Zhuo, Qi-Sheng Tian, Yan Jin, and Liang-Sheng Liao. Self-assembled high quality cspbbr3 quantum dot films toward highly

efficient light-emitting diodes. *ACS nano*, 12(9):9541–9548, (2018).

[142] Chen Wu, Yatao Zou, Tian Wu, Muyang Ban, Vincenzo Pecunia, Yujie Han, Qipeng Liu, Tao Song, Steffen Duhm, and Baoquan Sun. Improved performance and stability of all-inorganic perovskite light-emitting diodes by antisolvent vapor treatment. *Advanced Functional Materials*, 27(28):1700338, (2017).

[143] Shany Gamliel, Alex Dymshits, Sigalit Aharon, Eyal Terkieltaub, and Lioz Etgar. Micrometer sized perovskite crystals in planar hole conductor free solar cells. *The Journal of Physical Chemistry C*, 119(34):19722–19728, (2015).

[144] Mohan Ramesh, Karunakara Moorthy Boopathi, Tzu-Yen Huang, Yu-Ching Huang, Cheng-Si Tsao, and Chih-Wei Chu. Using an airbrush pen for layer-by-layer growth of continuous perovskite thin films for hybrid solar cells. *ACS applied materials & interfaces*, 7(4):2359–2366, (2015).

[145] Rebecca J. Sutton, Marina R. Filip, Amir A. Haghighirad, Nobuya Sakai, Bernard Wenger, Feliciano Giustino, and Henry J. Snaith. Cubic or orthorhombic? revealing the crystal structure of metastable black-phase cspbi3 by theory and experiment. *ACS Energy Letters*, 3(8):1787–1794, (2018).

[146] Arthur Marronnier, Guido Roma, Soline Boyer-Richard, Laurent Pedesseau, Jean-Marc Jancu, Yvan Bonnassieux, Claudine Katan, Constantinos C. Stoumpos, Mercouri G. Kanatzidis, and Jacky Even. Anharmonicity and disorder in the black phases of cesium lead iodide used for stable inorganic perovskite solar cells. *ACS nano*, 12(4):3477–3486, (2018).

[147] Mehmet Ozcan, Sercan Ozen, Gokhan Topcu, Mustafa M. Demir, and Hasan Sahin. Color-tunable all-inorganic cspbbr3 perovskites nanoplatelet films for photovoltaic devices. *ACS Applied Nano Materials*, 2(8):5149–5155, (2019).

[148] Jun Kang and Lin-Wang Wang. High defect tolerance in lead halide perovskite cspbbr3. *The journal of physical chemistry letters*, 8(2):489–493, (2017).

[149] Xiaolei Yang, Xingwang Zhang, Jinxiang Deng, Zema Chu, Qi Jiang, Junhua Meng, Pengyang Wang, Liuqi Zhang, Zhigang Yin, and Jingbi You. Efficient green light-emitting diodes based on quasi-two-dimensional composition and phase engineered perovskite with surface passivation. *Nature communications*, 9(1):1–8, (2018).

[150] Sercan Ozen, Fadıl Iyikanat, Mehmet Ozcan, G. Efsun Tekneci, Ismail Eren, Yiğit Sozen, and Hasan Sahin. Orthorhombic cspbi3 perovskites: Thickness-dependent structural, optical and vibrational properties. *Computational Condensed Matter*, page e00453, (2020).

[151] Shilpa N. Raja, Yehonadav Bekenstein, Matthew A. Koc, Stefan Fischer, Dandan Zhang, Liwei Lin, Robert O. Ritchie, Peidong Yang, and A. Paul Alivisatos. Encapsulation of perovskite nanocrystals into macroscale polymer matrices: enhanced stability and polarization. *ACS applied materials & interfaces*, 8(51):35523–35533, (2016).

[152] Ziyu Wang, Qingdong Ou, Yupeng Zhang, Qianhui Zhang, Hui Ying Hoh, and Qiaoliang Bao. Degradation of two-dimensional ch3nh3pbi3 perovskite and ch3nh3pbi3/graphene heterostructure. *ACS applied materials & interfaces*, 10(28):24258–24265, (2018).

[153] Guoxiong Su, Viktor G. Hadjiev, Phillip E. Loya, Jing Zhang, Sidong Lei, Surendra Maharjan, Pei Dong, Pulickel M. Ajayan, Jun Lou, and Haibing Peng. Chemical vapor deposition of thin crystals of layered semiconductor sns2 for fast photodetection application. *Nano letters*, 15(1):506–513, (2015).